X-RAY REFLECTION SPECTROSCOPY OF THE BLACK HOLE GX 339–4: EXPLORING THE HARD STATE WITH UNPRECEDENTED SENSITIVITY

The Astrophysical Journal, 813:84 (19pp), 2015 November 10 doi:10.1088/0004-637X/813/2/84

X-RAY REFLECTION SPECTROSCOPY OF THE BLACK HOLE GX 339–4: EXPLORING THE HARD STATE WITH UNPRECEDENTED SENSITIVITY

Javier A. García[1], James F. Steiner[1], Jeffrey E. McClintock[1], Ronald A. Remillard[2], Victoria Grinberg[2], and Thomas Dauser[3]
[1] Harvard-Smithsonian Center for Astrophysics, 60 Garden St., Cambridge, MA 02138, USA; javier@head.cfa.harvard.edu, jem@cfa.harvard.edu, jsteiner@head.cfa.harvard.edu
[2] MIT Kavli Institute for Astrophysics and Space Research, MIT, 70 Vassar St., Cambridge, MA 02139, USA; rr@space.mit.edu, grinberg@space.mit.edu
[3] Dr. Karl Remeis-Observatory and Erlangen Centre for Astroparticle Physics, Sternwartstr. 7, D-96049 Bamberg, Germany; thomas.dauser@sternwarte.uni-erlangen.de
Received 2015 March 1; accepted 2015 September 18; published 2015 October 30

ABSTRACT

We analyze *simultaneously* six composite *RXTE* spectra of GX 339–4 in the hard state comprising 77 million counts collected over 196 ks. The source spectra are ordered by luminosity and span the range 1.6%–17% of the Eddington luminosity. Crucially, using our new tool `pcacorr`, we re-calibrate the data to a precision of 0.1%, an order of magnitude improvement over all earlier work. Using our advanced reflection model `relxill`, we target the strong features in the component of emission reflected from the disk, namely, the relativistically broadened Fe K emission line, the Fe K edge, and the Compton hump. We report results for two joint fits to the six spectra: For the first fit, we fix the spin parameter to its maximal value ($a_* = 0.998$) and allow the inner disk radius $R_{\rm in}$ to vary. Results include (i) precise measurements of $R_{\rm in}$, with evidence that the disk becomes slightly truncated at a few percent of Eddington and (ii) an order-of-magnitude swing with luminosity in the high energy cutoff, which reaches >890 keV at our lowest luminosity. For the second fit, we make the standard assumption in estimating spin that the inner edge of the accretion disk is located at the innermost stable circular orbit ($R_{\rm in} = R_{\rm ISCO}$) and find $a_* = 0.95^{+0.03}_{-0.05}$ (90% confidence, statistical). For both fits, and at the same level of statistical confidence, we estimate that the disk inclination is $i = 48^\circ \pm 1^\circ$ and that the Fe abundance is super-solar, $A_{\rm Fe} = 5 \pm 1$.

Key words: accretion, accretion disks – atomic processes – black hole physics – line: formation – X-rays: individual (GX 339–4)

1. INTRODUCTION

GX 339–4 is one of the most thoroughly studied of the roughly 50 known black-hole X-ray binaries. Its orbital period is around 1.7 days, and for the best candidate period of 1.7557 days the mass function is $5.8 \pm 0.5\,M_\odot$ (Hynes et al. 2003). Like nearly all black hole binaries, the X-ray source is transient, having undergone more than a dozen outburst cycles since its discovery in the early 1970s by Markert et al. (1973). During a cycle, GX339–4 often exhibits all known X-ray states, which unfold in the canonical pattern (Remillard & McClintock 2006; Dunn et al. 2010). During the rising phase, the source can reach exceptional luminosities in the hard state, which is the focus of this paper.

The hard state is strongly dominated by a hard power-law component ($\Gamma \sim 1.6$). The thermal component, which contributes $\lesssim$20% of the 2–20 keV flux, is faint and cool ($kT \lesssim 0.2$ keV) compared to the thermal state (Remillard & McClintock 2006). The Fe K line is a ubiquitous spectral feature. Strong variability is a hallmark of the hard state (rms power >10% in the band 0.1–10 Hz), while quasi-periodic oscillations may be either present or absent. The state is associated with the presence of an AU-scale steady jet, and clear correlations between the radio and X-ray intensities are observed (Corbel et al. 2013). A major question for the hard state is the geometry of the corona: while there is significant evidence that the corona in the hard state is compact, it is quite unclear whether, e.g., it is advection-dominated accretion flow (ADAF)-like and quasi-spherical, hugs the disk, or originates at the base of a jet (Corbel et al. 2000; Shidatsu et al. 2011).

1.1. Controversy over the Location of the Disk's Inner Edge

In the thermal state, there is abundant evidence that the accretion disk is truncated near the innermost stable circular orbit (ISCO) (e.g., Gierliński & Done 2004; Penna et al. 2010; Steiner et al. 2010; Zhu et al. 2012). The standard paradigm for the faint hard state is that as the luminosity decreases the inner edge of the disk recedes from the ISCO, leaving a hot ADAF or other coronal flow (Narayan & Yi 1994; Narayan & McClintock 2008). While there is good evidence that at very low luminosities the disk is grossly truncated (for a review, see Narayan & McClintock 2008), the location of the inner edge relative to the ISCO for luminosities in the range ~0.1%–10% of Eddington is a hotly debated topic. With GX 339–4 as a principal test bed, two methods have been widely used to estimate the radius $R_{\rm in}$ of the inner edge of the disk in the hard state: (1) modeling the component of emission reflected from the disk, principally the Fe K line; and (2) fitting the continuum spectrum of the accretion disk. The former method, which is addressed in the following section, is the central topic of this paper.

Efforts to estimate the inner edge of the accretion disk in the low/hard state via disk reflection go back farther, but the first strong indication that disks may remain close to the ISCO in bright phases of the low/hard state was made by Miller et al. (2006b). Based on fits to the thermal component, a number of papers claim that there is an optically thick disk that extends inward to the ISCO in the hard state (Miller et al. 2006a, 2006b; Rykoff et al. 2007; Reis et al. 2009, 2010; Reynolds et al. 2010). This claim is strongly contested by Done et al. (2007) and Done & Diaz Trigo (2010); the claim is all the more questionable when one considers that self-consistent disk

coronal models (e.g., Steiner et al. 2009) return larger values of the inner-disk radius. More recently, Miller and coworkers have invoked extreme values of the spectral hardening factor in making the case for an untruncated hard-state disk (Reynolds & Miller 2013; Salvesen et al. 2013). This evidence for the presence of such a disk does not appear to us compelling given the difficulties of obtaining accurate estimates of $R_{\rm in}$ by modeling a faint, cool ($kT \lesssim 0.2$ keV) thermal component that is strongly Comptonized and cut off by interstellar absorption.

1.2. Reflection Spectroscopy

The reflection spectrum results from the reprocessing of high-energy coronal photons in the optically thick accretion disk. The result is a rich spectrum of radiative recombination continua, absorption edges, and fluorescent lines, most notably the Fe K complex in the 6–8 keV energy range. This reflected radiation leaves the disk carrying information on the physical composition and condition of the matter in the strong fields near the black hole. The Fe K emission line (and other fluorescent lines) are broadened and shaped by Doppler effects, light bending, and gravitational redshift. By modeling the reflection spectrum, one can estimate both the disk inclination and the dimensionless spin parameter $a_* = cJ/GM^2$ ($-1 \leqslant a_* \leqslant 1$). In measuring a_*, one estimates the radius of the inner edge of the accretion disk and identifies it with the radius of the ISCO, $R_{\rm ISCO}$, which simply and monotonically maps to a_* (Bardeen et al. 1972). For the three canonical values of the spin parameter, $a_* = +1$, 0 and -1, $R_{\rm ISCO} = 1\,M$, $6\,M$ and $9\,M$ (for $c = G = 1$), respectively.

The reflection model most widely used in the past for both general application and measuring black hole spin is REFLIONX (Ross & Fabian 2005). Recently, an improved reflection model has been developed, RELXILL,[4] which is based on the reflection code XILLVER (García & Kallman 2010; García et al. 2011, 2013, 2014a), and the relativistic line-emission code RELLINE (Dauser et al. 2010, 2013, 2014). Compared to REFLIONX, RELXILL incorporates a superior treatment of radiative transfer and Compton redistribution, and it allows for the angular dependence of the reflected spectrum. Furthermore, by implementing the routines of the photoionization code XSTAR (Kallman & Bautista 2001), RELXILL provides an improved calculation of the ionization balance. At the same time, limitations of the model include assuming that the density of the disk is independent of vertical height, that the illuminating radiation strikes the disk at a fixed angle of 45°, and that apart from Fe all the elemental abundances are assumed to be solar. The results presented in this paper were derived using RELXILL to model the relativistically blurred reflection component from the inner disk and XILLVER to model a distant reflector.

It is important to appreciate the faintness of the reflected features that are crucial for probing effects in the regime of strong gravity, the features that one relies on for estimating $R_{\rm in}$ and constraining black hole spin. For example, in the spectrum of GX 339–4, even the most prominent feature, the Fe K line, has a typical equivalent width of ∼0.1 keV, and the peak intensity of the line is only about 10% of the local continuum (Section 3). Sensitivity to such faint features requires both high-count spectra and a well-calibrated detector.

[4] http://www.sternwarte.uni-erlangen.de/research/relxill

1.3. The Special Quality of This Study

The principal detector on board the *Rossi X-ray Timing Explorer* (*RXTE*) was the Proportional Counter Array (PCA), which was comprised of five nearly identical Proportional Counter Units (PCUs), each with an effective area of 1600 cm^2 and with sensitivity from 2–60 keV. Despite the limited spectral resolution of the instrument (≈17% at 6 keV) the archive of PCA data amassed during the *RXTE* mission (1995–2012) continues to be preeminent for the synoptic study of stellar-mass black holes. A few-dozen bright black holes were observed daily during their outburst cycles with typical exposure times of a few ks. Some 15,000 individual spectra were obtained with a net total exposure time of 30 Ms (1 year). In this paper, we report the results of our analysis of six hard-state spectra of GX 339–4, each a summation of dozens of individual exposures (Section 3). For the spectrum obtained at maximum luminosity ($L/L_{\rm Edd} = 17\%$) with an exposure time of 46 ks, the total number of counts is 40 million and the counts-per-keV in the continuum at 6.4 keV is 4.4 million, while the total number of counts in the Fe K line region (3–10 keV) is 28 million.

A limitation of the PCA, which has not allowed the implied statistical precision to be realized in modeling data, has been the appreciable ∼1% uncertainties in the detector response (Jahoda et al. 2006; Shaposhnikov et al. 2012). We have overcome this limitation by developing a calibration tool, called PCACORR, that increases the sensitivity of the *RXTE* PCA detector to faint spectral features—such as the Fe K line/edge–by up to an order of magnitude (García et al. 2014b). By applying PCACORR to a large number of spectra for three black holes, we found that the tool improved the quality of all the fits, and that the improvement was dramatic for spectra with $\gtrsim 10^7$ counts. The tool allows one to achieve a precision of ∼0.1% rather than ∼1%, thereby making full use of spectra of bright sources with $\sim 10^6$ counts per channel.

Consequently, our study of the reflection spectrum of GX 339–4 greatly improves on earlier studies using the PCA, such as that by Plant et al. (2015). A limitation of PCA data is its modest resolution, while its major advantage is its freedom from the problematic effects of pileup, which is commonly a serious problem in analyzing and interpreting data for bright sources obtained using CCD detectors (see Section 6.1.3). Another advantage of the PCA, which has only recently been matched by *NuSTAR*, is its high-energy coverage, which allows observations of both the Fe K region and the Compton hump using a single detector.

This paper is organized as follows: Section 2 describes the observations and data reduction, and Section 3 outlines our procedure for combining the individual spectra into six composite spectra. The luminosities of these spectra, which we refer to throughout as Spectra A–F, range over an order of magnitude. Fitting the spectra individually, while emphasizing the importance of correcting the data using the PCACORR tool, is the subject of Section 4. Our key results appear in Section 5. Therein, we describe how we fit Spectra A–F simultaneously, first fixing the spin parameter and letting the inner-disk radius vary, and then allowing the spin parameter to vary while fixing the inner radius at the ISCO. We discuss our results in Section 6 and offer our conclusions in Section 7.

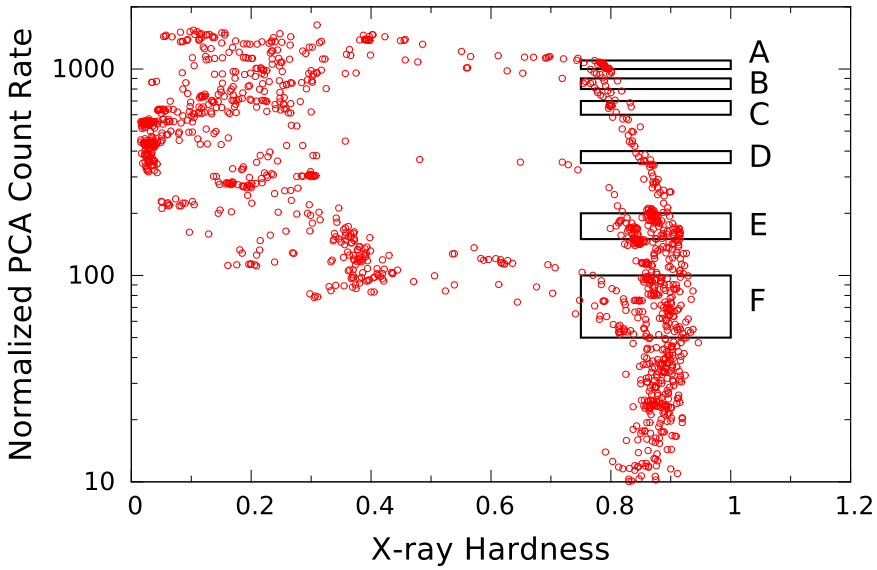

Figure 1. Hardness-intensity diagram for all PCU-2 *RXTE* observations of GX 339–4. The vertical axis shows the raw PCU-2 count rate (for reference, 1 Crab $\approx$ 2600 counts s^{-1}), a proxy for the X-ray intensity and luminosity. Plotted on the horizontal axis is the hardness ratio *HR* defined as the ratio of source counts at 8.6–18 keV to the counts at 5–8.6 keV. Following further the conventions of Remillard & McClintock (2006), the hard-state data considered exclusively in this paper are defined to have $HR > 0.75$. The six boxes labeled A–F define the data sets we sum to create Spectra A–F, which are used in our analysis throughout the paper.

2. OBSERVATIONS AND DATA REDUCTION

Our reduction and analysis of the *RXTE* PCA data are detailed in García et al. (2014b), which follows the procedures of McClintock et al. (2006). The data were obtained in "Standard 2" mode and segmented into contiguous intervals with exposure times ranging from 300 to 5000 s. Background spectra, which were derived using `pcabackest` and the model `pca_bkgd_cmvle_eMv20111129.mdl`, were subtracted from the data. Response files were generated using `pcarmf` (version 11.7) and the energy-to-channel conversion table (version *e05v04*) described in Shaposhnikov et al. (2012). Throughout, we analyze just the data collected using the best-calibrated detector, PCU-2, which also provides the richest data set.

As a crucial final step, we apply the tool PCACORR (García et al. 2014b) to the data and thereby calibrate the detector to a precision of $\sim$0.1%; we include a systematic error of this magnitude in all our data analysis. This step greatly enhances the sensitivity of the detector (Section 4.3) to the reflection features that are our focus.

Figure 1 presents a hardness-intensity diagram, PCA count rate versus PCA hardness ratio *HR*, for all 1471 *RXTE* PCU-2 observations of GX 339–4 obtained between 1996 July 26 and 2011 April 5. The hard-state data considered exclusively in this paper are defined to have $HR > 0.75$. In order to boost the signal-to-noise, we define the six boxes A–F shown in Figure 1. Each box contains a number of spectra, all of them corresponding to roughly the same source intensity. We combine all the spectra within a box using the procedures described in Section 3; importantly, we do not combine spectra obtained during different outburst cycles. Except for Box A, which is comprised of observations taken during the 2002 outburst, all the other boxes contain observations taken during the 2010 outburst. Ultimately, we produce six master spectra (A–F), one for each box.

3. COMBINING SPECTRA

We now outline our procedure for combining the individual spectra in a box to create Spectra A–F in such a way as to eliminate small variations in the power-law index under the assumption that the reflection features are unaffected by small changes in the continuum. For each box separately, we first fitted the individual spectra to a simple absorbed power-law (`Tbabs*powerlaw`) using a fixed hydrogen column density of $N_{\rm H} = 3 \times 10^{21}\,{\rm cm}^{-2}$, which is similar to the expected column in the direction of GX 339–4 (Kalberla et al. 2005). No evidence for a thermal component was found in any of the spectra. The fits were performed in the 3–45 keV band where the Fe K features are most pronounced.[5] We then created individual residual spectra (data counts minus model) and summed them, thereby greatly enhancing the residual features present in these spectra.

Figure 2 shows the residual spectra for the six boxes. The striking features in each spectrum are the Fe K line and the K edge, which are revealed with precision in these high signal-to-noise spectra. Surprisingly, the overall structure of the residuals are in all cases quite similar, despite the factor of $\sim$10 spread in luminosity (Figure 1). Upon closer examination, however, one sees that the line width, the position of the edge, and the shape of the Compton hump differ to some degree among the boxes. This point is discussed in more detail in Section 5.1.

We now use these residuals to create Spectra A–F, which constitute our prime data set. To be specific, consider the creation of Spectrum A: for box A we generate a single template continuum spectrum using the average values of the fit parameters Γ and the normalization N. This spectrum is generated synthetically using the `fakeit` task in XSPEC; its net exposure time is the sum of the exposure times of all the 23 individual spectra in box A. Finally, we add this continuum

[5] Inclusion or exclusion of the 4–7 keV band was found to have a negligible effect on our final results.

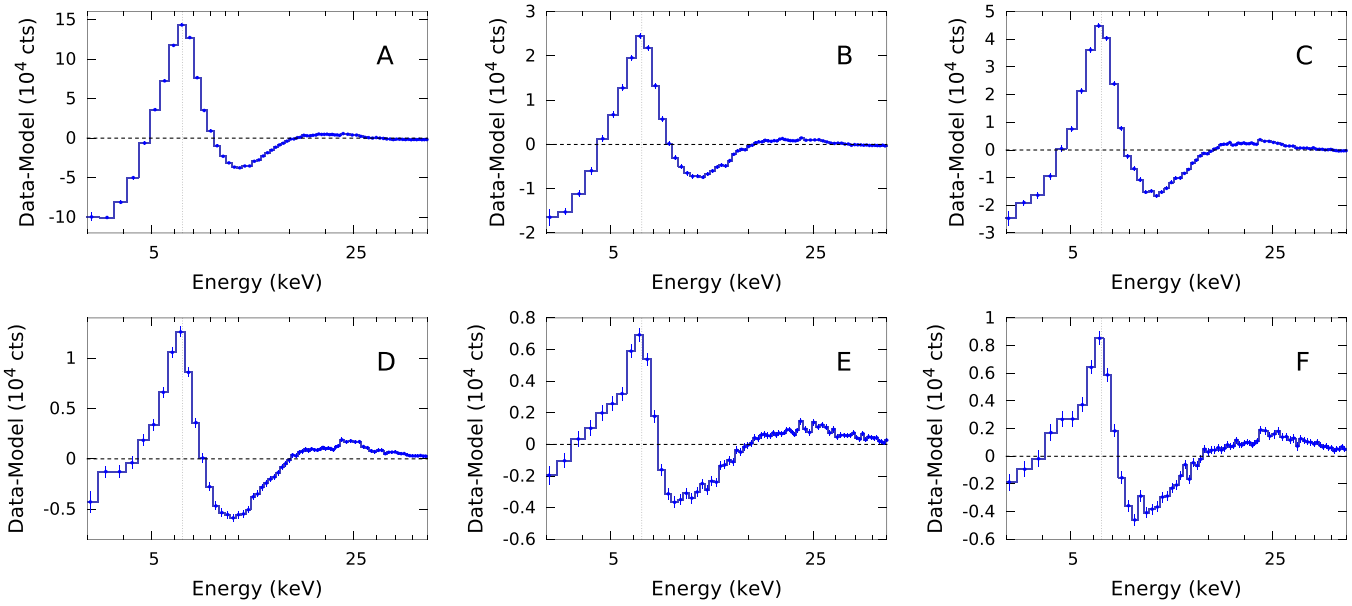

Figure 2. Residuals (data-minus-model) are computed for each box (defined in Figure 1) by subtracting an absorbed power-law fit to the individual spectra in the box. The extreme statistical precision results from summing millions of counts, ranging from ∼28 million for Box A to ∼3 million for Box F (3–10 keV). Note that the spectra are all scaled differently; e.g., the peak signal for the highest-luminosity Box A is ∼15 times greater than for the lowest-luminosity Box F. Remarkably, the appearance of the spectra is quite insensitive to luminosity.

Table 1
Properties of Spectra A–F and the Boxes Defined in Figure 1

Spectrum	$L/L_{\rm Edd}$ (%)[a]	Count Rate	# Spectra	$\langle\Gamma\rangle$	$\langle N\rangle$	Exp. (ks)
A	17.3	1000–1100	23	1.72 ± 0.01	2.12 ± 0.11	45.7
B	14.2	800–900	7	1.75 ± 0.03	1.81 ± 0.10	10.3
C	11.9	600–700	11	1.69 ± 0.01	1.22 ± 0.06	27.0
D	7.9	350–400	7	1.61 ± 0.60	0.60 ± 0.03	15.7
E	3.9	150–200	18	1.52 ± 0.01	0.23 ± 0.02	24.6
F	1.6	50–100	43	1.59 ± 0.08	0.11 ± 0.03	72.7

Note.
[a] Eddington-scaled luminosities assuming $D = 8$ kpc and $M = 10\,M_\odot$ (corresponding to $L_{\rm Edd} = 1.\,25 \times 10^{39}$ erg s^{-1}), and based on the fluxes computed over the 1–100 keV band using the model and fit parameters summarized in Table 3.

spectrum to its corresponding summed residual spectrum to complete the generation of Spectrum A.

The resulting spectrum is superior to that obtained by simply summing the individual spectra directly because it seamlessly eliminates the effects of small differences in the power-law index and normalization among the spectra. The mean power-law parameters and other information describing these six spectra, which are hereafter our focus, are summarized in Table 1. We compute the luminosity for a spectrum using our model fluxes in the 1–100 keV band and assuming a distance of $D = 8$ kpc and black hole mass of $M = 10\,M_\odot$ (for details, see Footnote *a* to Table 1).

4. FITTING SPECTRA A–F INDIVIDUALLY

The residual plots in Figure 2 unambiguously demonstrate that a strong reflected component is present, which is widely attributed to the illumination of the disk by a hot corona. Invoking this paradigm, we proceed to fit each of the six spectra using our physically motivated reflection code `relxill` v0.2 g (García et al. 2014a). As before, Galactic absorption is modeled using `Tbabs` with fixed column density ($N_{\rm H} = 3 \times 10^{21}$ cm^{-2}). For the `Tbabs` model (Wilms et al. 2000), we used the Anders & Grevesse (1989) set of solar abundances and the Verner et al. (1996) photoelectric cross sections.

We fit Spectra A–F in turn to a succession of four models; the final adopted model in each case yields a good fit with $\chi^2/\nu \sim 1$. Table 2 provides detailed information on the quality of the fit for each spectrum and each model. In Figure 3, we show for Spectrum A with 4×10^7 counts—the most challenging case—residual plots for the progression of the four models, which we now describe.

Model 0: `Tbabs*powerlaw`. An absorbed power-law model, which is clearly deficient, prominently displays the principal reflection features, the Fe K line/edge and Compton hump, in the residuals (Figure 3).

Model 1: `Tbabs*relxill`. A greatly improved fit to all six spectra is achieved by replacing the power-law with our fully relativistic reflection model. For simplicity and to achieve definiteness, we fix the spin to its extreme value of $a_* = 0.998$ and assume the canonical dependence of disk emissivity with radius, namely $\propto r^{-3}$. This model already delivers fits of reasonable quality (Table 2). Some pronounced residual features remain, which are most evident for the most luminous case, Spectrum A (Figure 3). Specifically, two apparent absorption features flank the Fe K line at ∼5.6 and

Table 2
Statistics of the Individual Fits to Spectra A–F

Spectrum	Model	χ^2	ν	χ^2_ν	$\Delta\chi^2/\Delta\nu$
A	0	25094.90	69	363.694	···
	1	299.07	63	4.747	4132.64
	2	151.07	62	2.437	148.00
	3	67.82	60	1.130	41.63
B	0	7653.27	69	110.917	···
	1	117.00	63	1.857	1256.05
	2	81.16	62	1.309	35.84
	3	54.14	60	0.902	13.51
C	0	11849.29	70	169.276	···
	1	142.44	64	2.226	1951.14
	2	93.21	63	1.480	49.23
	3	68.68	61	1.126	12.27
D	0	4880.44	70	69.721	···
	1	89.91	64	1.405	798.42
	2	41.36	63	0.657	48.55
	3	35.69	61	0.585	2.84
E	0	2552.13	70	36.459	···
	1	116.40	65	1.791	487.15
	2	65.97	64	1.021	50.43
F	0	2311.81	70	33.026	···
	1	63.17	65	0.9719	449.73
	2	63.17	64	0.9870	0.0

~7.2 keV. Other features are also present at higher energies in the region of the Compton hump (~20–45 keV).

Model 2: `Tbabs*(relxill+xillver)`. The residuals are significantly reduced by including an *unblurred* reflection component via `xillver`. Physically, this reflector could be cold material in a wind or in the outer region of a flared disk (see below). The `xillver` parameters are linked to those of `relxill` with two exceptions: The ionization parameter was fixed at its minimum value, $\log \xi = 0$, and the Fe abundance was fixed to solar (i.e., $A_{\rm Fe} = 1$). Linking the Fe abundance results in a significantly worse fit and a compromise value of abundance that is midway between the low value required by the unblurred component and the super-solar value required by the blurred component (see Section 6.1.4). This result, and the uncertain origin of the unblurred component, motivate our choice of solar Fe abundance for the distant reflector. We have no good explanation for the different Fe abundances required in fitting the blurred and unblurred reflection components. Further discussion on the Fe abundance is presented in Section 6.1.4.

Inclusion of the `xillver` component, which introduces only one new free parameter, namely its normalization, quite significantly improves the fit to all the spectra except Spectrum F, which has the fewest counts. While the `xillver` component improves the fit at low energies and in the region of the Compton hump, a strong residual feature remains at ~7.2 keV (Figure 3).

Model 3: `Tbabs*(relxill+xillver)*gabs`. We model the remaining residual feature near 7.2 keV phenomenologically as absorption using a single Gaussian. The addition of this component improves the fits substantially for Spectra A–C, i.e., those with many counts, while it has only a marginal effect for Spectrum D and a negligible effect for Spectra E and F (Table 2). As expected, its importance is greatest for Spectrum A where it completely eliminates the strong 7.2 keV residual feature (Figure 3) and produces a very good fit to this spectrum, despite its extreme statistical precision (4×10^7 total counts), with an allowance for systematic error of only 0.1% (Section 2).

It is important to note that the inclusion of the 7.2 keV feature has a significant effect on some important model parameters. In particular, we find that including the Gaussian component (Model 3) increases the inclination and decreases the inner-disk radius by about 4 degrees and 20%, respectively, compared to excluding the component. The changes in the other fit parameters are relatively much smaller. We adopt Model 3 as our fiducial model for all six spectra, thereby assuming that the 7.2 keV absorption feature has a physical origin. While it is beyond the scope of this work to establish a definite physical interpretation of the feature, we now briefly consider some plausible explanations.

4.1. The 7.2 keV Absorption Feature and the Efficacy of the `xillver` Component

We first consider the likely possibility that the absorption feature is largely an artifact related to the uncertain energy resolution of the PCA. We then discuss the one plausible physical explanation for the feature known to us, namely that it is produced by absorption in a highly ionized wind. Finally, we consider the role of the `xillver` component not only in modeling the residual features near the Fe K line, but also its role in improving the fit quite generally.

4.1.1. On the Accuracy of the PCA Energy Resolution

The presence of residual absorption features bracketing the Fe line at ~5.6 and ~7.2 keV suggests the possibility that the PCA resolution may be better than assumed in generating the PCU-2 response. We have explored this possibility for Spectrum A. We test the effects of slight changes in the value assumed for the detector resolution by moderately smoothing the data, with the results shown in Figure 4. The smoothing is accomplished using a Gaussian kernel operating over the detector channels; the parameter f specifies the width of the Gaussian as a percent of the channel width. Accordingly, the curve in Figure 4 labeled $f = 0$ is unsmoothed, while the curves labeled $f = 40$ and $f = 50$ correspond to degrading the resolution of the data by 0.9% and 1.5% at 6.4 keV.

Although this approximate approach to artificially tuning the detector resolution does not eliminate the residuals flanking the Fe line, it does significantly reduce their strength. The test demonstrates that at this extreme level of statistical precision the fit to a line feature is very sensitive to the value assumed for the detector resolution. Specifically, if one assumes that the nominal value of resolution for the unsmoothed case ($f = 0$) at 6 keV is 17.0%, then the net resolution for $f = 50$ is 17.3% (i.e., the additional blurring has a width of one-half channel, equivalent to ~0.2 keV at 6.4 keV, which is combined in quadrature with the nominal resolution width). Meantime, the resolution of the PCA is not known to sufficient accuracy to discriminate such fine differences (N. Shaposhnikov 2015, private communication). This suggests that the residuals near the Fe line may result from the PCA resolution being slightly better than assumed in modeling the detector response. However, this test is inconclusive. To properly assess the importance of tuning the resolution, one must carry out a

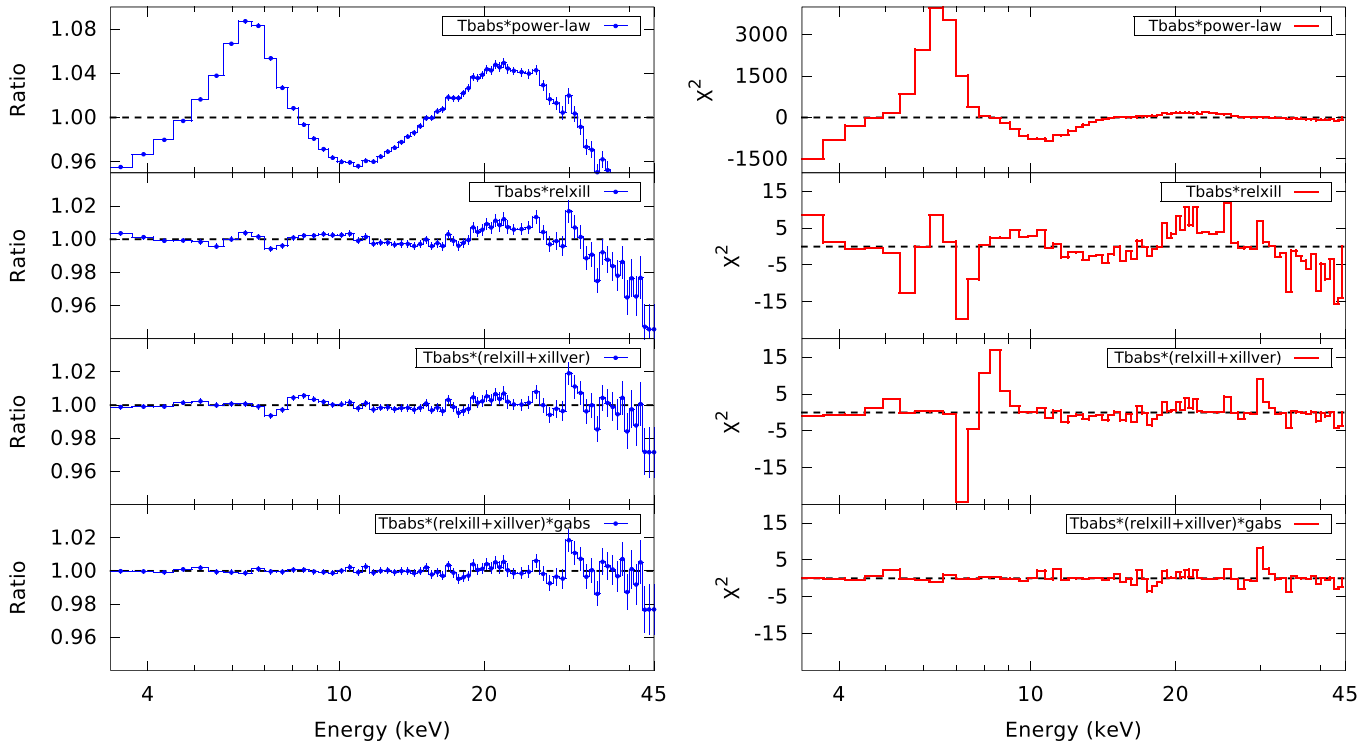

Figure 3. Data-to-model ratio (*left*) and contributions to χ^2 (*right*) for Spectrum A resulting from fitting a sequence of four models. From top to bottom, the models increase in completeness and competence, starting with an absorbed power-law model to which, incrementally, is added a blurred reflection component (`relxill`); unblurred reflection (`xillver`); and a Gaussian absorption line `gabs`. The comparable residual plots for the other five spectra are qualitatively similar.

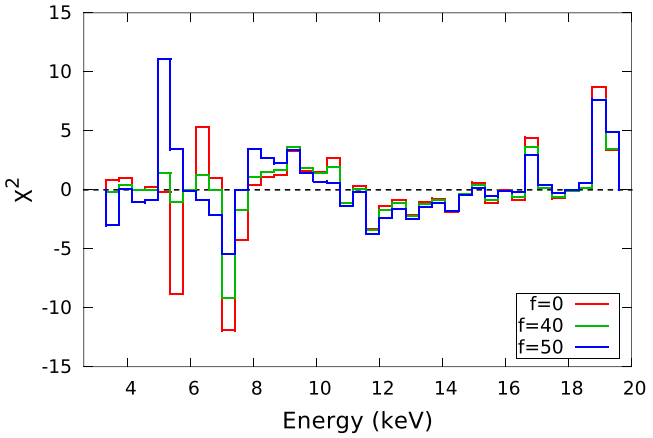

Figure 4. Residual plots (data-model) illustrating the extreme sensitivity in fitting the Fe K line to the value assumed for the energy resolution of PCU-2. The residuals are for fits to Spectrum A using Model 1 (`Tbabs*relxill`). The resolution of the data have been slightly degraded by convolving them with a Gaussian whose smoothing width is characterized by the parameter f: The cases $f = 40$ (green) and $f = 50$ (blue) correspond to decreases in the resolution of 0.9% and 1.5%, respectively, and $f = 0$ (red) is the unsmoothed case.

systematic analysis using the PCA calibration software, which is beyond the scope of this paper.

4.1.2. On the Possibility that the Feature Originates in a Highly Ionized Wind

If the 7.2 keV feature is not an instrumental artifact, a potentially plausible explanation is that it originates in a highly ionized wind that envelops the primary source. Disk winds have been observed in many black hole binary systems, particularly at high accretion rates (e.g., Miller et al. 2006c; Neilsen et al. 2012; Ponti et al. 2012). We investigated this possibility by replacing the `gabs` component by the photo-ionized warm absorber model (`warmabs`). We forced the Fe Lyα line at ~6.9 keV to be the dominant feature by setting the ionization parameter to its maximum value ($\log \xi = 5$). We linked the Fe abundances of `warmabs` and `relxill` while the abundances of all the other elements remain at solar. The fitted blueshift of the Fe Lyα required to model the 7.2 keV feature is $z = 0.0576 \pm 0.0101$, which corresponds to an outflow velocity of $v = 1.7 \times 10^4$ km s^{-1}. The model provides a good fit ($\chi^2_\nu = 1.17$), which is very comparable to that achieved using Model 3 (see the top-left panel of Figure 5 for details and a comparison of the residuals). However, this interpretation seems unlikely on physical grounds due to the extreme column density required by the warm absorber, namely, $N_{\rm H}^{\rm abs} = (7.7 \pm 0.2) \times 10^{23}$ cm^{-2}. If one links the `warmabs` Fe abundance to that of the `xillver` component (i.e., $A_{\rm Fe} = 1$), the fit pegs at the hard limit of the `warmabs` model (10^{24} cm^{-2}).

4.1.3. On the Inclusion of the Unblurred Reflection Component

Our initial motivation for including the unblurred `xillver` component of reflection was the presence of the ~5.6 and ~7.2 keV residual features flanking the Fe line. However, as Figure 3 makes clear, while the `xillver` component effectively eliminated the low-energy feature, it actually enhanced the 7.2 keV feature. The simplest ad hoc phenomenological approach to eliminating both features is to include a pair of Gaussian absorption lines in our model, which we did, fixing the widths of the Gaussians to 0.01 keV and allowing the energy and strength of each line to vary. While

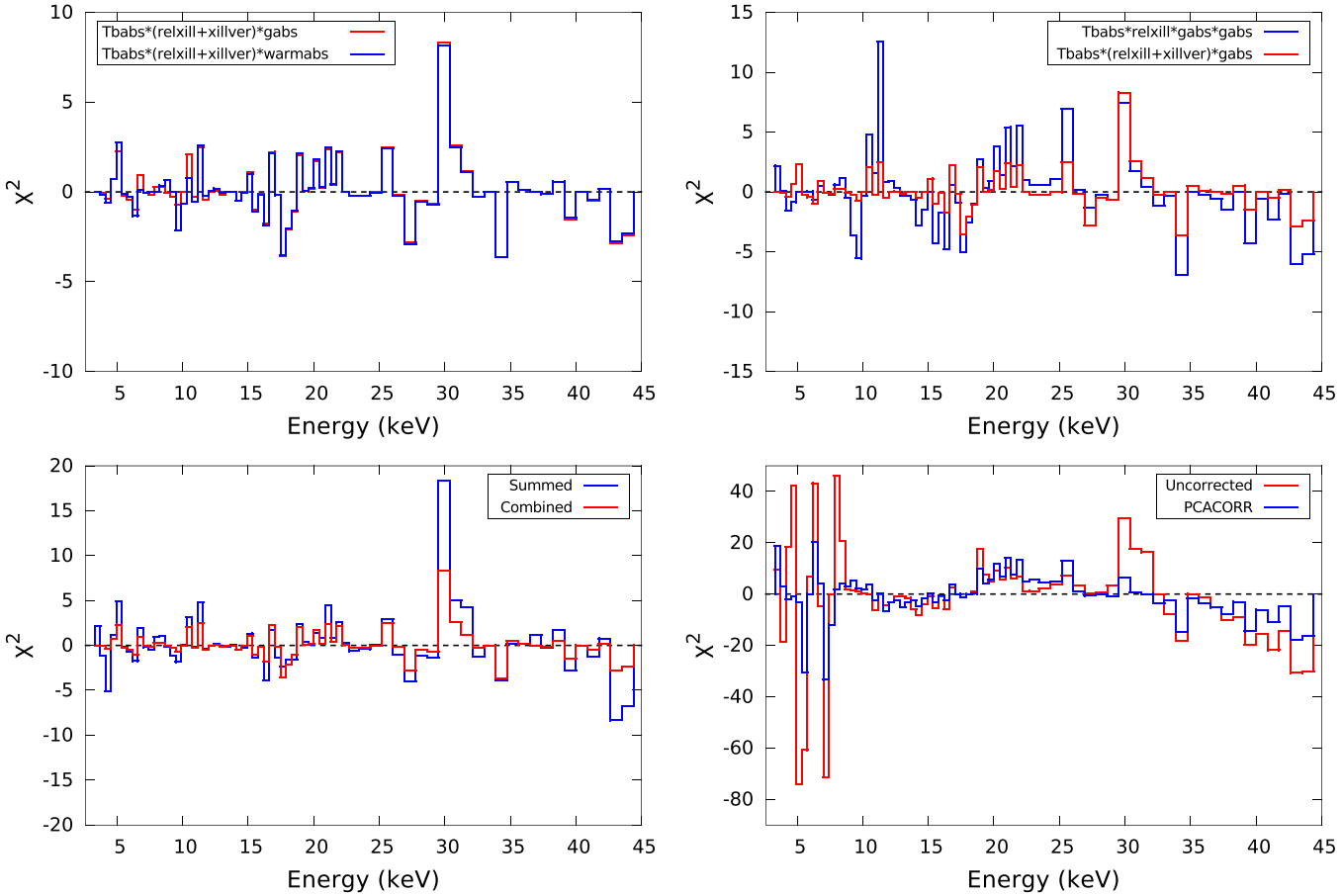

Figure 5. Comparative plot showing contributions to the total χ^2 (data-model) for each channel for fits to Spectrum A. (*Top-left*) The red curve was computed for our adopted Model 3 (`Tbabs*(relxill+xillver)*gabs`) and is identical to the plot shown in the lower-right panel in Figure 3. The blue curve is for an alternative model that substitutes the warm absorber model `wabs` for `gabs` in our adopted Model 3. The alternative model provides a good fit to the data: $\chi^2 = 69.06$ for 59 dof ($\chi^2_\nu = 1.130$); compare χ^2 values for Model 3 in Tables 3 and 4. (*Top-right*) The red curve was computed for our adopted Model 3 and is identical to the plot shown in the lower-right panel in Figure 3. The blue curve is for an alternative model that replaces the unblurred (`xillver`) reflection component by a second Gaussian absorption line at ∼5.6 keV (blue), which results in a distinctly inferior fit. As this residual plot shows, Model 3 performs better at almost all energies. (*Bottom-left*) Fits of our adopted Model 3 for two cases: (1) A direct sum of the 23 spectra in Box A (blue), and (2) a fit to Spectrum A (red), which was prepared by combining the spectra according to the procedures described in Section 3. While the model parameters are consistent for the two cases, Spectrum A provides a superior fit, as this comparison of the residuals makes clear. (*Bottom-right*) Fits using Model 1 (`Tbabs*relxill`) for two cases: (1) the 23 individual spectra that comprise Spectrum A are corrected using the PCACORR tool (blue) and (2) they are left uncorrected (red). In this instance only, all systematic errors have been zeroed to most clearly illustrate the effect of applying PCACORR to the data.

this model (`Tbabs*relxill*gabs*gabs`) does clean up the ∼5.6 keV and ∼7.2 keV features, the quality of the fit, $\chi^2_\nu = 2.36$ ($\chi^2 = 139.25$ for 59 dof), is much poorer than that achieved with Model 3, $\chi^2_\nu = 1.13$ ($\chi^2 = 67.82$ for 60 dof), which uses `xillver` and a single Gaussian. As the top-right panel of Figure 5 makes clear for the stringent case of Spectrum A, the latter model not only does a better job cleaning up the pair of targeted residual features, it is also more effective at improving the fit at most other energies as well. We consider this strong evidence for the presence in GX 339–4 of a distant reflector.

4.2. Comparing Combined versus Summed Spectra

As discussed in Section 3, we combined the individual spectra in order to increase our sensitivity to the reflection features while minimizing the effects of jitter in the power-law index. To verify the procedures we used in combining spectra, we compare the results of fitting our Spectrum A to those obtained by fitting a spectrum created by summing directly all the spectra in Box A.[6] Applying PCACORR and fitting both spectra with our adopted model (i.e., `Tbabs*(relxill +xillver)*gabs`), we find that the model parameters are all consistent. However, the fit to the summed spectrum is of significantly lower quality ($\Delta\chi^2 = 62.97$) than the fit to Spectrum A created using the procedures described in Section 3. Furthermore, as shown in the bottom-left panel of Figure 5, the residuals for the summed spectrum are larger in almost every energy channel. These results demonstrate that our method of combining the individual spectra significantly improves the quality of the fit.

4.3. The Importance of Applying the PCACORR Tool

As fully described in García et al. (2014b) and discussed in Section 1.3, the PCACORR tool greatly reduces the effects of instrumental features in PCA spectra, thereby making it

[6] The effects of changes in the detector response are negligible because the 23 observations were all made during a 10-day interval.

Table 3
Results for JF-I: Fit Parameters for Model 3, `const*Tbabs*(relxill+xillver)*gabs`, with Fixed Maximum Spin a_* and Free $R_{\rm in}$

Model	Parameter	Spectrum A	Spectrum B	Spectrum C	Spectrum D	Spectrum E	Spectrum F
Tbabs	$N_{\rm H}$ ($\rm cm^{-2}$)			$(7.0 \pm 1.0) \times 10^{21}$			
relxill	a_*			0.998			
relxill	i (deg)			48.4 ± 1.1			
relxill	$A_{\rm Fe}$			$4.6^{+0.5}_{-0.3}$			
relxill	$N_{\rm r}$			$1.48^{+0.05}_{-0.03}$			
gabs	E (keV)			$7.19^{+0.04}_{-0.06}$			
Constant		1	0.91 ± 0.04	0.71 ± 0.02	0.36 ± 0.01	0.16 ± 0.01	0.08 ± 0.01
relxill	$R_{\rm in}$ ($R_{\rm ISCO}$)	$1.7^{+0.2}_{-0.3}$	$1.5^{+0.4}_{-0.2}$	$1.8^{+0.1}_{-0.2}$	$2.1^{+0.3}_{-0.5}$	$2.7^{+0.5}_{-1.5}$	$3.7^{+0.7}_{-1.0}$
relxill	Γ	1.620 ± 0.013	1.682 ± 0.016	1.672 ± 0.013	1.628 ± 0.015	1.588 ± 0.010	$1.648^{+0.007}_{-0.012}$
relxill	$\log\xi$	$3.31^{+0.03}_{-0.07}$	3.24 ± 0.07	$3.12^{+0.07}_{-0.03}$	$3.031^{+0.020}_{-0.013}$	2.02 ± 0.17	$2.05^{+0.26}_{-0.10}$
relxill	$E_{\rm cut}$	97^{+3}_{-5}	129 ± 10	179 ± 14	660^{+130}_{-170}	>840	>890
relxill	$R_{\rm f}$	0.21 ± 0.02	0.22 ± 0.03	0.21 ± 0.03	$0.34^{+0.04}_{-0.05}$	0.31 ± 0.03	$0.31^{+0.02}_{-0.03}$
xillver	N_x	$0.27^{+0.02}_{-0.03}$	0.25 ± 0.04	0.25 ± 0.04	$0.34^{+0.04}_{-0.05}$	<0.05	<0.03
gabs	Strength	$0.021^{+0.009}_{-0.007}$	$0.029^{+0.017}_{-0.012}$	0.036 ± 0.016	$0.05^{+0.07}_{-0.03}$	$0.08^{+0.16}_{-0.05}$	$0.14^{+0.10}_{-0.05}$
	$L/L_{\rm Edd}$(%)	17.3	14.2	11.9	7.9	3.9	1.6
	χ^2			402.49			
	ν			379			
	χ^2_ν			1.06			

Note. For the given model components, the parameters from top to bottom are: hydrogen column density ($N_{\rm H}$); dimensionless spin parameter ($a_* = cJ/GM^2$, where J is the angular momentum of the black hole); inclination of the inner disk (i); iron abundance with respect to its solar value ($A_{\rm Fe}$); normalization of the blurred reflection component plus power-law continuum ($N_{\rm r}$); energy of the absorption Gaussian centroid (E); constant multiplicative factor between spectra; inner-disk radius ($R_{\rm in}$), with $R_{\rm ISCO} = 1.237\ R_g$ for $a_* = 0.998$ ($R_g = GM/c^2$); power-law photon index (Γ); log of the ionization parameter ($\xi = 4\pi F_x/n$, where F_x is the ionizing flux and n is the gas density); high-energy cutoff ($E_{\rm cut}$); reflection fraction ($R_{\rm f}$, ratio of the reflected flux to that in the power-law, in the 20–40 keV band); normalization of the distant (unblurred) reflection (N_x); strength of the absorption Gaussian; X-ray luminosity in terms of Eddington (see notes in Table 1); goodness of the fit (χ^2); number of degrees of freedom (ν); goodness of the fit per degree of freedom ($\chi^2_\nu = \chi^2/\nu$). Uncertainties are based on a 90% confidence level.

possible to achieve good fits to high-count spectra at the 0.1% level of statistical precision. The bottom-right panel in Figure 5 demonstrates the importance of applying the tool to Spectrum A, with its 4×10^7 counts. The figure compares residuals for a fit to uncorrected data to one using PCACORR-corrected data. To most clearly illustrate the power of PCACORR, we use Model 1 (`Tbabs*relxill`) and set the systematic errors to zero. Concerning the ∼5.6 keV and ∼7.2 keV features flanking the Fe K line, we note that they are present prior to the application of PCACORR, which confirms that they are not introduced by the correction. The key message of the bottom-right panel in Figure 5 is the degree to which PCACORR diminishes these features and others, especially those below 10 keV and the one near 30 keV, a feature that is likely related to the detector Xe K-edge (Shaposhnikov et al. 2012; García et al. 2014b).

5. FITTING SPECTRA A–F SIMULTANEOUSLY

In order to achieve the strongest possible constraints on the key model parameters, we fitted Spectra A–F simultaneously. This composite data set is an assemblage of 106 individual PCA/PCU-2 spectra of GX 339–4 in the hard state. The total number of counts is 77 million, 34 million of which are in the 3–10 keV Fe K band.

All fits are performed using Model 3 (`const*Tbabs*(relxill+xillver)*gabs`). To accommodate the order-of-magnitude range of luminosity, we included a normalization constant that is unity for Spectrum A and floats for Spectra B–F. Where sensible, key physical parameters are tied: the spin a_* of the black hole; inclination i of the system; line-of-sight column density $N_{\rm H}$; Fe abundance $A_{\rm Fe}$; and the normalization of the relativistic reflection component $N_{\rm r}$ (see Table 3). Given the uncertain origin of the absorption feature near 7.2 keV, which we model as a Gaussian, we also tie the central energy of this component while allowing its normalization to vary from spectrum to spectrum. The width of the Gaussian was fixed at 0.01 keV in all the spectra. Like the Gaussian normalization, all other model parameters are allowed to vary independently.

Despite the extreme signal-to-noise of the composite spectrum, we must impose some additional assumptions in order to simultaneously constrain both the spin parameter a_* and the radius of the inner edge of the accretion disk $R_{\rm in}$. This is because these two quantities, which manifest almost indistinguishably in the red wing of the Fe K line profile, are extremely degenerate (Dauser et al. 2013). Therefore, we have conducted two complementary analyses, which we will refer to as JF-I and JF-II, where JF signifies that these are joint fits (i.e., simultaneous) to Spectra A-F (rather than the fits to Spectrum A alone that are featured in earlier sections). For JF-I, our aim is to constrain $R_{\rm in}$, and we therefore keep the spin fixed at its maximum value of $a = 0.998$. For JF-II, we tie the spin parameter for the six spectra and fit for it, while fixing the inner edge of the disk at the ISCO; i.e., $R_{\rm in} = R_{\rm ISCO}$. We follow the guidelines of Fabian et al. (2012) and fix the emissivity index to its canonical value of 3; for both JF-I and JF-II, we do not attempt to fit for this parameter because of the PCA's limited spectral resolution. This choice is motivated by several JF-I and JF-II tests we performed that returned values of the emissivity index that were always $\lesssim 4$.

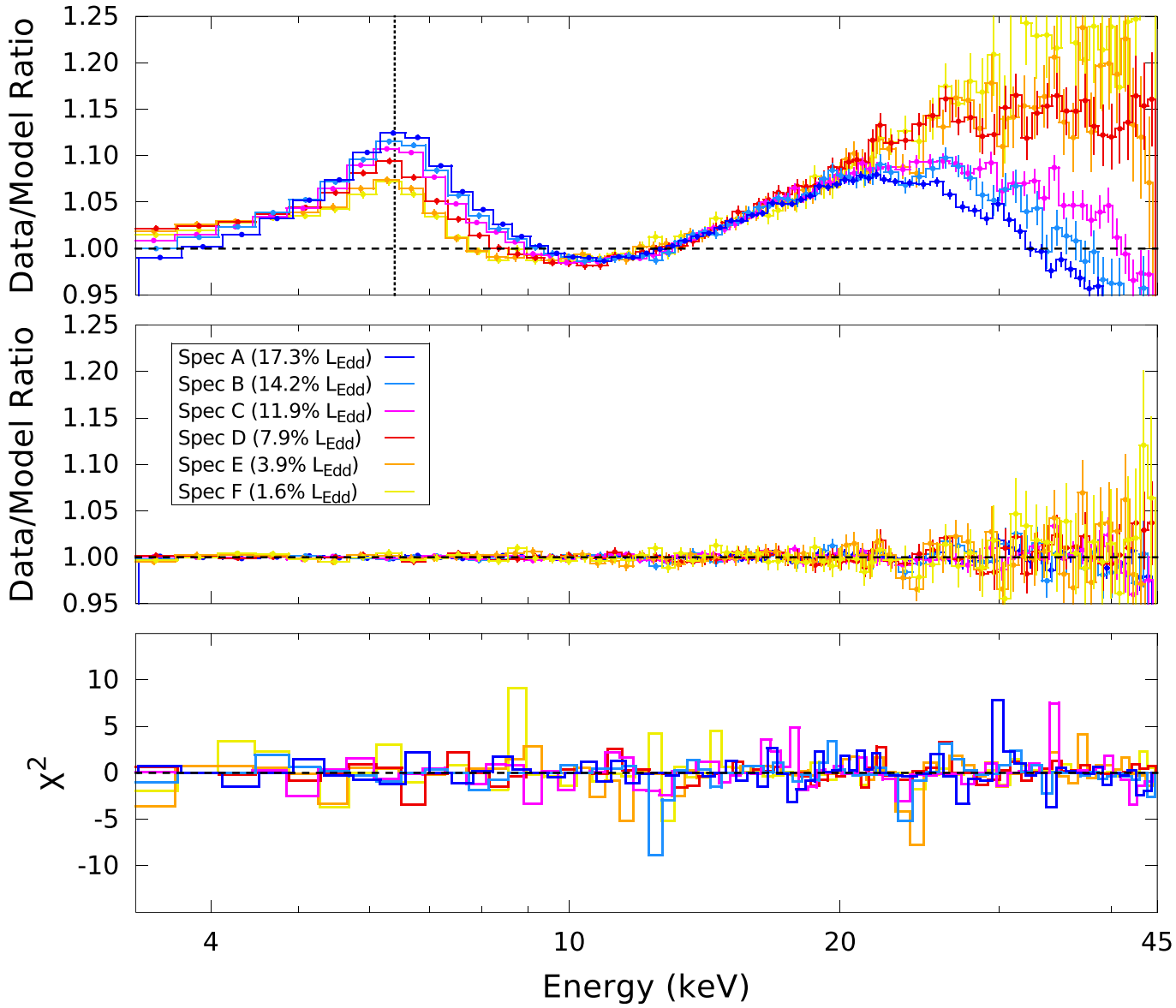

Figure 6. Simultaneous fit to Spectra A–F comprising a total of 106 individual spectra and 77 million counts. (*Top*) Ratio plots for a joint fit (JF-I) using Model 0, the simple absorbed power-law model, which strikingly reveal the principal signatures of reflection. (*Middle*) Ratio plots for these same data obtained by fitting our canonical Model 3 (`Tbabs*(relxill+xillver)*gabs`). This model produces an excellent fit with $\chi^2_\nu = 1.06$. (*Bottom*) Contributions to the total χ^2 (data-model), again for Model 3 and the same data.

The number of free fitting parameters is large, 52 for JF-I and 47 for JF-II. The complexity of the analysis dictated our approach: We performed Markov Chain Monte-Carlo (MCMC) runs using the EMCEE-HAMMER Python package (Foreman-Mackey et al. 2013), which implements affine-invariant sampling. MCMC methods are powerful for high-dimensional analysis. Specifically, they enable an efficient exploration of parameter space and determine a posterior probability structure for the model of interest.

5.1. Joint Fit I: Fixed Spin and Variable Inner Radius

A principal goal of our study is to track the radius of the inner edge of the disk $R_{\rm in}$ as the luminosity varies by an order of magnitude (i.e., over the range 1.6%–17% of Eddington; Table 1). As discussed in Section 1.1, a question of great interest is whether the inner disk is truncated in the hard state at low luminosities and, if so, to what extent. In order to be maximally sensitive to a disk that is only slightly truncated, we fix the spin to its maximum allowed value, namely $a_* = 0.998$. In so doing, our focus is on determining how $R_{\rm in}$ trends with luminosity rather than obtaining accurate estimates of this parameter. We note that most spin determinations in the literature (which assume $R_{\rm in} = R_{\rm ISCO}$) suggest that the spin is high (see Section 6.1.3).

Figure 6 shows the fit residuals for JF-I for two cases: (1) The top panel shows a data-to-model ratio for a fit to Model 0, i.e., the simple absorbed power-law model used to produce the residual plot for a fit to Spectrum A only (which is shown in the left-top panel of Figure 3). This simple fit prominently displays the reflection features, which are strong for all six spectra. The profile of the Fe K line shows moderate variations among the spectra. As the luminosity increases, so does the intensity of the

Table 4
Results for JF-II: Fit Parameters for Model 3, `const*Tbabs*(relxill+xillver)*gabs`, with a_* free and $R_{\rm in} = R_{\rm ISCO}$

Model	Parameter	Spectrum A	Spectrum B	Spectrum C	Spectrum D	Spectrum E	Spectrum F
Tbabs	$N_{\rm H}$ ($\rm cm^{-2}$)			$(5.9^{+0.6}_{-1.9}) \times 10^{21}$			
relxill	a_*			$0.95^{+0.03}_{-0.05}$			
relxill	i (deg)			$47.8^{+0.9}_{-1.4}$			
relxill	$A_{\rm Fe}$			$5.4^{+1.9}_{-0.5}$			
relxill	$N_{\rm r}$			$1.44^{+0.04}_{-0.08}$			
gabs	E (keV)			7.23 ± 0.08			
Constant		1	$0.90^{+0.03}_{-0.04}$	$0.71^{+0.02}_{-0.03}$	0.37 ± 0.02	0.17 ± 0.01	0.08 ± 0.01
relxill	$R_{\rm in}$ ($R_{\rm ISCO}$)			1			
relxill	Γ	$1.604^{+0.010}_{-0.027}$	1.658 ± 0.018	$1.651^{+0.015}_{-0.022}$	$1.62^{+0.02}_{-0.04}$	$1.578^{+0.009}_{-0.013}$	$1.637^{+0.009}_{-0.013}$
relxill	logξ	3.33 ± 0.03	3.35 ± 0.04	$3.16^{+0.10}_{-0.05}$	$3.05^{+0.04}_{-0.02}$	$1.96^{+0.12}_{-0.21}$	$2.0^{+0.2}_{-0.2}$
relxill	$E_{\rm cut}$	92^{+2}_{-6}	118 ± 8	160^{+12}_{-16}	440^{+230}_{-110}	>830	>940
relxill	$R_{\rm f}$	0.20 ± 0.01	$0.20^{+0.02}_{-0.01}$	0.20 ± 0.02	$0.27^{+0.03}_{-0.05}$	$0.25^{+0.05}_{-0.03}$	$0.28^{+0.02}_{-0.04}$
xillver	N_x	$0.23^{+0.05}_{-0.02}$	0.26 ± 0.04	0.24 ± 0.05	0.13 ± 0.06	0.08 ± 0.06	<0.09
gabs	Strength	$0.024^{+0.009}_{-0.007}$	$0.028^{+0.018}_{-0.011}$	$0.037^{+0.016}_{-0.012}$	$0.04^{+0.03}_{-0.02}$	0.025 ± 0.014	$0.020^{+0.017}_{-0.009}$
	$L/L_{\rm Edd}$(%)	17.3	14.2	11.9	7.9	3.9	1.6
	χ^2			418.66			
	ν			384			
	χ^2_ν			1.09			

Note. For the given model components, the parameters from top to bottom are: hydrogen column density ($N_{\rm H}$); dimensionless spin parameter ($a_* = cJ/GM^2$, where J is the angular momentum of the black hole); inclination of the inner disk (i); iron abundance with respect to its solar value ($A_{\rm Fe}$); normalization of the blurred reflection component plus power-law continuum ($N_{\rm r}$); energy of the absorption Gaussian centroid (E); constant multiplicative factor between spectra; inner-disk radius ($R_{\rm in}$); power-law photon index (Γ); log of the ionization parameter ($\xi = 4\pi F_x/n$, where F_x is the ionizing flux and n is the gas density); high-energy cutoff ($E_{\rm cut}$); reflection fraction ($R_{\rm f}$, ratio of the reflected flux to that in the power-law, in the 20–40 keV band); normalization of the distant (unblurred) reflection (N_x); strength of the absorption Gaussian; X-ray luminosity in terms of Eddington (see notes in Table 1); goodness of the fit (χ^2); number of degrees of freedom (ν); goodness of the fit per degree of freedom ($\chi^2_\nu = \chi^2/\nu$). Uncertainties are based on a 90% confidence level.

line (cf. Figure 2). Additionally, the blue wing of the line extends to higher energies for the high luminosity spectra, which could be evidence for a shift in the Fe K edge caused by an increase in the ionization of the gas. There are obvious changes at high energies among the spectra, which are likely due to the evolution of the high-energy cutoff with luminosity. (2) Of chief interest, the middle and bottom panels of Figure 6 show the residuals for our adopted Model 3 (for $a_* = 0.998$).

Model 3 performs remarkably well for all spectra as indicated by the goodness of fit, $\chi^2_\nu = 1.06$, and also by the uniformly ergodic appearance of the residuals across the energy band. The fit results are summarized in Table 3. A key result, which is discussed in detail in the following section, is evidence that the disk is moderately—but significantly—truncated at the lowest luminosities that can be effectively explored using *RXTE* (i.e., at a few percent of Eddington).

5.2. Joint Fit II: Constraining the Spin of the Black Hole

In order to obtain constraints on black hole spin using either leading method, reflection spectroscopy or continuum fitting, one must assume that $R_{\rm in} = R_{\rm ISCO}$ (e.g., McClintock et al. 2014; Reynolds 2014). In performing JF-II, we make this assumption *for all six spectra* in order to constrain the spin of the black hole. Doing so allows us to obtain a precise estimate of spin: $a_* = 0.95^{+0.03}_{-0.05}$ at 90% confidence. As the summary of results in Table 4 shows, the other parameters are quite close to those obtained in JF-I (Table 3), and the goodness of fit is of very comparable quality: $\chi^2_\nu = 1.09$. Given the extreme statistical precision, the residual spectra (data/model and χ^2) for JF-II (not shown) are essentially indistinguishable by eye from the spectra for JF-I, which are shown in Figure 6.

Concerning our spin estimate and the fundamental assumption that $R_{\rm in} = R_{\rm ISCO}$, we again note that JF-I provides evidence for disk truncation at our lowest luminosities.[7] Meantime, these low-luminosity spectra are included in computing our single, tied JF-II estimate of spin. The incorporation of disk truncation effects (which we have ignored) would imply an even higher spin value than is quoted above.

6. DISCUSSION

The MCMC runs utilized 120 (JF-I) and 100 (JF-II) "walkers," each navigating a chain with a length of 100,000 elements, after having been initialized in a cluster distributed about the best fit. The first 50,000 elements of each walker were discarded in the "burn-in" phase during which the chain reaches its stationary state. The typical autocorrelation length, which is the interval over which the chain forgets its previous location, was several thousand elements; the corresponding net number of independent samples of the parameter space was $\sim 10^4$. From the full distribution, we trivially obtain a probability distribution for any given set of parameters of interest by marginalizing over all the parameters that were outside that set. Flat priors were adopted for all model parameters.

[7] Furthermore, our JF-I results are consistent with some small degree of truncation even for our higher-luminosity data.

Table 5
Compilation of Literature Estimates of $R_{\rm in}$ Obtained by Fitting Reflection Models to Hard-state Spectra of GX 339–4

Satellite	Instrument	$L/L_{\rm Edd}$ (%)	$R_{\rm in}$ (R_g)	i (deg)	q	High-energy?	References
XMM-Newton	EPIC-pn (TM)[a]	1.42	684^{+301}_{-378}	42^{+11}_{-6}	3	Yes	(1)
	⋯	⋯	972^{+28}_{-643}	36^{+3}_{-6}	3	Yes	(2)
	⋯	⋯	110^{+80}_{-40}	60	3	No	(3)
	⋯	⋯	150^{*}_{-50}	60	3	No	(4)
	EPIC-MOS	3.25	5 ± 0.5	20^{+5}_{-10}	3	Yes	(5)
	⋯	⋯	$2.04^{+0.07}_{-0.02}$	$20_{-1.3}$	3.16 ± 0.5	Yes	(6)
	EPIC-pn	⋯	10 ± 2	27 ± 3	3	Yes	(7)
	⋯	⋯	60^{+40}_{-20}	60	3	Yes	(8)
	EPIC-pn (TM)[a]		318^{+165}_{-74}	42^{+11}_{-6}	3	Yes	(1)
	⋯	⋯	125^{+21}_{-51}	36^{+3}_{-6}	3	Yes	(2)
	⋯	⋯	89^{+55}_{-23}	60	3	No	(3)
	⋯	⋯	128^{+73}_{-43}	60	3	No	(4)
	⋯	10.2	155^{+139}_{-53}	42^{+11}_{-6}	3	Yes	(1)
	⋯	⋯	72^{+42}_{-21}	36^{+3}_{-6}	3	Yes	(2)
	⋯	⋯	2.2^{*}	60	3	No	(3)
	⋯	⋯	47^{+10}_{-7}	60	3	No	(4)
	⋯	<0.05	21^{+17}_{-9}	30^{+5}_{-4}	3	No	(14)
	⋯	<0.05	27^{+6}_{-6}	30^{+5}_{-4}	3	No	(14)
	⋯	<0.05	16^{+7}_{-4}	30^{+5}_{-4}	3	No	(14)
Suzaku	XIS0,1,3/PIN	0.14	>65	18	2–3	Yes	(9)
	⋯	⋯	>798	42^{+11}_{-6}	3	Yes	(1)
	⋯	⋯	>745	36^{+3}_{-6}	3	Yes	(2)
	⋯	⋯	190^{+170}_{-90}	50	2.3	Yes	(10)
	⋯	⋯	>180	20	3	Yes	(11)
	⋯	0.13	>30	20	3	Yes	(11)
	⋯	0.19	>10	20	3	Yes	(11)
	⋯	0.25	>70	20	3	Yes	(11)
	⋯	0.60	32^{+33}_{-19}	20	3	Yes	(11)
	⋯	0.91	$7.0^{+1.1}_{-1.3}$	20	3	Yes	(11)
	⋯	2.0	$13.3^{+6.4}_{-6.0}$	46 ± 8	2.3 ± 0.1	Yes	(10)
Swift	XRT	1.33	$3.6^{+1.4}_{-1.0}$	20	3.2 ± 0.6	Yes	(12)
	⋯	⋯	$6.7^{+9.1}_{-2.3}$	20	3	Yes	(13)
	⋯	0.46	<10	20	3.1 ± 0.4	Yes	(12)
	⋯	⋯	$3.6^{+1.9}_{-0.9}$	20	3	Yes	(13)
	⋯	1.08	$12.8^{+19.8}_{-9.0}$	20	3	Yes	(13)
	⋯	1.12	$6.9^{+9.1}_{-3.7}$	20	3	Yes	(13)
	⋯	1.68	$19.5^{+25}_{-8.5}$	20	3	Yes	(13)
	⋯	2.23	$16.3^{+11.7}_{-5.2}$	20	3	Yes	(13)
	⋯	5.21	$19.7^{+12.1}_{-6.5}$	20	3	Yes	(13)

Note. (1) Plant et al. (2015) implementing `xillver`, (2) Plant et al. (2015) implementing `reflionx`, (3) Kolehmainen et al. (2014), (4) Kolehmainen et al. (2014) including a notch feature at ∼9 keV, (5) Miller et al. (2006b), (6) Reis et al. (2008), (7) Done & Diaz Trigo (2010), (8) Done & Diaz Trigo (2010) with fixed inclination, (9) Tomsick et al. (2009) (10) Shidatsu et al. (2011), (11) Petrucci et al. (2014), (12) Tomsick et al. (2008), (13) Allured et al. (2013), (14) Plant et al. (2014b).
[a] TM = Timing Mode.

6.1. The Four Intrinsic Parameters of the System

We first discuss four parameters that are global for GX 339–4 (i.e., the same for all six spectra), namely, the Galactic hydrogen column density $N_{\rm H}$, the spin parameter a_* of the black hole, the inclination i, and the Fe abundance $A_{\rm Fe}$. The entries for these (and all other) parameters estimated in the MCMC analysis given in Tables 3 and 4 are 90% minimum-width confidence intervals about the posterior maxima.

6.1.1. Hydrogen Column Density

Despite the limited low-energy coverage of the PCA, the hydrogen column density is well-constrained in both JF-I and JF-II to $N_{\rm H} = (6.5^{+0.8}_{-1.5}) \times 10^{21}\,{\rm cm}^{-2}$ (Tables 3 and 4), which is consistent with other estimates in the literature, including (in units of $10^{21}\,{\rm cm}^{-2}$) 4–6 (Kong et al. 2000); 6 (Zdziarski et al. 2004); 5.4 (Shidatsu et al. 2011); and 5–8 (Méndez & Klis 1997).

6.1.2. Inclination of the Inner Disk

Previous estimates of inclination, which have been obtained by modeling the reflected component, run the gamut (see Table 5). Three papers using the same *XMM-Newton* and *RXTE* data uniformly report low values: Miller et al. (2006b) and Reis et al. (2008) obtained $i = 20^{+5}_{-15}$ deg and $i \lesssim 20°$, respectively,

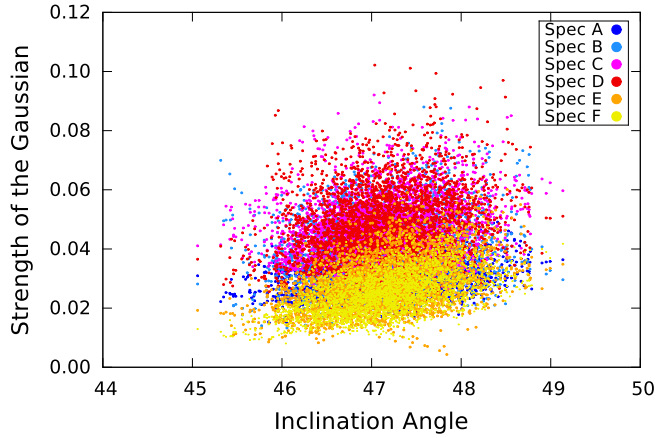

Figure 7. Probability density map for the strength of the Gaussian absorption component (`gabs`) and the inclination angle from our MCMC analysis for JF-II. While the inclination is tied between the six spectra A–F, the strength of the `gabs` component is free to vary. The distribution for each spectrum is coded by color. Only weak correlation is observed, with the `gabs` component becoming slightly stronger as the inclination increases and as the luminosity decreases.

while Done & Diaz Trigo (2010), using a different strategy for reducing the data, found $i \sim 20°$–$27°$. A much larger inclination, $i = 46 \pm 8$ degrees, was determined by Shidatsu et al. (2011) using *Suzaku* data. All of these results were obtained using the `reflionx` models (Ross & Fabian 2005). Recently, Plant et al. (2015) fitted simultaneously *XMM-Newton* and *Suzaku* data sets using both `reflionx` and `xillver` and reported two estimates of inclination: $i = 36^{+3}_{-6}$ deg and $i = 42^{+11}_{-6}$ deg. In a different work, Plant et al. (2014b) analyzed three low/hard state observations of GX 339–4 using a recent version of the `relxill` model and found $i = 30^{+5}_{-4}$ deg, a result that may be biased because it relies solely on low-energy *XMM-Newton* data.

In JF-I, we obtained a tight constraint on inclination, $i = 48.^{\circ}4 \pm 1.^{\circ}1$ (Table 3), a result that is consistent with that obtained in JF-II (Table 4). Note that the `relxill` and `xillver` models used here properly treat the angular distribution of the reflected radiation, unlike earlier reflection models, which only provided an angle-averaged solution (García et al. 2014a).

As an aside, if one makes the usual assumption that the spin of the black hole is aligned with the orbital angular momentum vector (Fragos et al. 2010; Steiner & McClintock 2012), then the lower estimates of inclination discussed above imply implausibly large values of black hole mass based on the Hynes et al. (2003) estimate of the mass function: e.g., $M \sim 5.8/\sin^3 i \sim 100\,M_{\odot}$ for $i \sim 25°$. Meanwhile, our inclination implies $M \sim 15\,M_{\odot}$, consistent with the range of values observed for stellar-mass black holes (Özel et al. 2010; Farr et al. 2011).

The inclination angle is largely determined by the shape and position of the blue wing of the Fe K line, which in our fits is somewhat affected by the inclusion—or exclusion—of the Gaussian absorption feature. The energy of this feature was linked in all six spectra and constrained to 7.23 ± 0.08 keV (Table 4), while the normalization was free to vary. Figure 7, based on our MCMC analysis, shows that while the strength of the `gabs` component does increase by a factor of ∼2 with decreasing luminosity, it only weakly interplays with inclination. This implies that this component, whose origin is uncertain (Section 4.1), has at most a modest affect on our estimate of inclination.

6.1.3. Black Hole Spin

The spin of the black hole has been estimated via reflection modeling using three independent data sets: $a_* = 0.939 \pm 0.004$ using *XMM-Newton*/EPIC-MOS plus *RXTE* spectral hard-state data (Miller et al. 2006b; Reis et al. 2008); $a_* = 0.93 \pm 0.02$ using *XMM-Newton*/EPIC-pn plus *RXTE* spectral data in the very high (or steep power-law) state (Miller et al. 2004; Reis et al. 2008); and $a_* = 0.93 \pm 0.01$ (statistical) ± 0.04 (systematic) using *Suzaku* data (Miller et al. 2008). The corresponding estimates of inclination were all low ($i \sim 10°$–$20°$) implying implausibly high estimates of black hole mass assuming spin–orbit alignment (Section 6.1.2).

There is considerable uncertainty associated with these estimates of spin and inclination because of the effects of pileup, i.e., the arrival of two or more photons in the same or adjacent CCD pixel within a single frame time. For example, Done & Diaz Trigo (2010), analyzing precisely the same hard-state *XMM-Newton*/EPIC-MOS data as Miller et al. (2006b) and Reis et al. (2008), conclude that the high spin reported by Miller et al. and Reis et al. is the result of severe pileup effects; using PN Timing-mode data (presumably unaffected by pileup), Done & Diaz Trigo (2010) report evidence for a narrow Fe line and a truncated disk. Meantime, Miller et al. (2010) rebut the conclusions of Done and Díaz Trigo. As a second example, the high spin reported by (Miller et al. 2008) based on their analysis of *Suzaku* data (see above), is challenged by Yamada et al. (2009) who find—using the same data set—evidence for a truncated disk and no need to invoke a rapidly spinning black hole.

Kolehmainen & Done (2010) applied the alternative continuum-fitting method to disk-dominated *RXTE* data collected during three different outbursts of GX 339–4. This method relies on accurate knowledge of the mass, distance, and inclination of the system, all of which are highly uncertain for GX 339–4. Using approximate bounds on these parameters, Kolehmainen & Done obtained "a strict upper limit" on the spin of $a_* < 0.9$, which they claim is inconsistent with the spin estimates obtained by modeling the reflection spectrum.

A chief virtue of the PCA data upon which we rely is its freedom from the confusing effects of pileup. A further virtue is the abundance of data, which allows us to track the behavior of GX 339–4 over a range of luminosity, as well as to reach extreme (∼0.1%) levels of statistical precision. By assuming that the inner radius of the disk always remains at the ISCO (JF-II; Section 5.2), we established a firm constraint on the spin at $a_* = 0.95^{+0.03}_{-0.05}$ (90% confidence) while obtaining a precise estimate of the inclination, $i = 47.8^{+0.9}_{-1.4}$ degrees. Our spin result is in accord with the earlier Fe-line estimates, but our inclination estimate is distinctly different, and more in line with expectation (Section 6.1.2).

The results of our MCMC analysis allow us to search for possible degeneracies of the spin parameter with other fit parameters. Figure 8 shows for JF-II spin probability distributions for three key parameters: (1) the inclination angle, which affects the blue wing of the line; (2) the Fe abundance, which affects the strength of both the line and edge; and (3) the strength of the Gaussian absorption, which also could affect the blue wing of the line. While there is no evidence for a

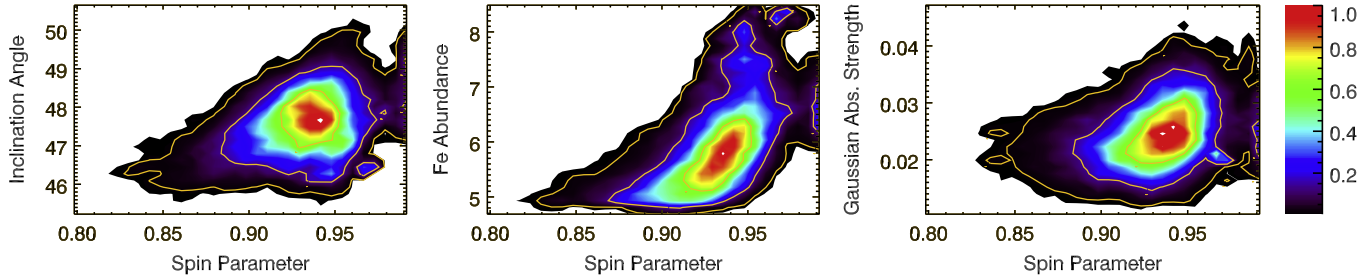

Figure 8. Probability contours from our MCMC analysis of JF-II for the spin parameter and three other parameters of interest: inclination angle (*left*), Fe abundance (*middle*), and the strength of the Gaussian absorption component (`gabs`) for Spectrum A (*right*). A modest positive correlation is observed between the Fe abundance and the spin parameter.

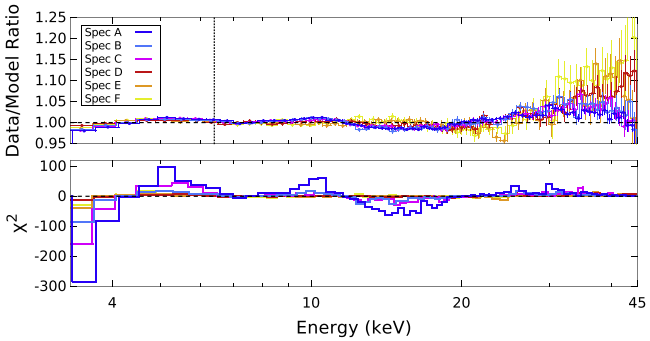

Figure 9. Spectral fitting results, similar to JF-I, but here fixing the Fe abundance to the solar value ($A_{\rm Fe} = 1$). The top and bottom panels show, respectively, a ratio plot and contributions to χ^2. This model fails to fit jointly the three principal reflection features (Fe K line and edge and the Compton hump), most noticeably for the higher-luminosity spectra, and the fit is unacceptable ($\chi^2_\nu = 9.9$). A vertical dashed line marks the 6.4 keV rest-frame energy of the Fe K line.

substantial correlation between the spin and the inclination or the strength of the Gaussian, there is indication of a moderate positive correlation with the Fe abundance. From this positive correlation, it follows that an increase in Fe abundance will produce a diminished inner radius for fits performed with a fixed spin and variable $R_{\rm in}$ (Section 6.3).

6.1.4. Fe Abundance

The Fe abundance for the blurred reflection component (`relxill`) is surprisingly high: $4.6^{+0.5}_{-0.3}$ and $5.4^{+1.9}_{-0.5}$ in solar units for JF-I and JF-II, respectively (Tables 3 and 4). Most studies have merely assumed that the abundance is solar, while Allured et al. (2013) fitted *Swift*/*RXTE* hard-state data and also found a super-solar abundance: $A_{\rm Fe} = 2.4^{+1.47}_{-0.62}$. The high abundance results directly from the remarkable strength of the Fe K line/edge relative to the Compton hump (top panel of Figure 6), which is usually the highest-amplitude feature in the reflection spectrum. A lower Fe abundance underpredicts the strength of the line/edge required to fit the Compton hump. Thus, our ability to constrain the Fe abundance is likely a consequence of our broad bandpass that provides high-sensitivity coverage of all the principal reflection features, from the Fe K line on through complete coverage of the Compton hump. This quality of coverage is not provided by *XMM-Newton* data (even when *RXTE* data with a floating normalization are included) which may explain why others have not reported a super-solar Fe abundance.

Quantitatively, forcing the Fe abundance to the solar value ($A_{\rm Fe} = 1$) results in a grossly unacceptable fit with $\chi^2_\nu = 9.9$ and large residuals across the PCA band (Figure 9), while the inner-disk radius grows by about a factor of 10 compared to the fit with variable Fe abundance. We tried several alternative models (e.g., varying the emissivity index) in an unsuccessful attempt to find an acceptable model with lower Fe abundance. We note that fits to *NuSTAR* data for the most recent outburst of GX 339–4 likewise require a large Fe abundance (Fuerst et al. 2015).

The Fe abundance has an influence on the shape of the Fe K line, and it may therefore in turn affect such parameters of interest as the inclination or inner-disk radius. Moreover, the abundance also alters the continuum photoelectric opacity at higher energies, which modifies the depth of the Fe K edge and the red side of the Compton hump. These effects, which are subtle, are driving our fits because of the unprecedented signal-to-noise we have achieved. We shall return to this point in Section 6.3.

We conclude that super-solar Fe abundance is a strong and inescapable requirement of these data. At the same time, the data also require the unblurred (distant) reflection to have moderate—near-solar—Fe abundance. In our tests, fitting the spectrum with the most counts (Spectrum A), we found that adopting a single abundance for both blurred and unblurred components (i.e., `relxill` and `xillver`) results in $A_{\rm Fe} \sim 3.6$, an intermediate value between `relxill` ($A_{\rm Fe} \sim 5$), and the low value required for the `xillver` component. Though this approach may be intuitively more satisfying, it is strongly rejected by the data, with an increase in χ^2 of ∼55. The effect of linking the abundances is to decrease the importance of the `xillver` component by reducing its normalization parameter from ∼0.2 to ∼0.07. An inspection of the residual contributions to χ^2 (lower panel of Figure 9) reveals that the quality of the fit is degraded not only in the Fe K region but over the entire energy band. In summary, we find strong empirical evidence for the presence of an unblurred reflection component whose Fe abundance is much less than that of the blurred component.

At the same time, there is no obvious reason why the inner-disk abundances should be so high. We note that similar physical processes may be occurring in AGN, since large Fe abundances are likewise found in many cases when fitting relativistic reflection models (Fabian 2006), with 1 H 0707–495 being a prime example (Dauser et al. 2012; Kara et al. 2015). Possibly, an unknown physical effect is being overlooked in current models that is artificially driving the Fe abundance to high values. For example, Reynolds et al. (2012) proposed that radiative levitation of Fe ions in the accretion disk atmosphere could cause an apparent enhancement of their abundance.

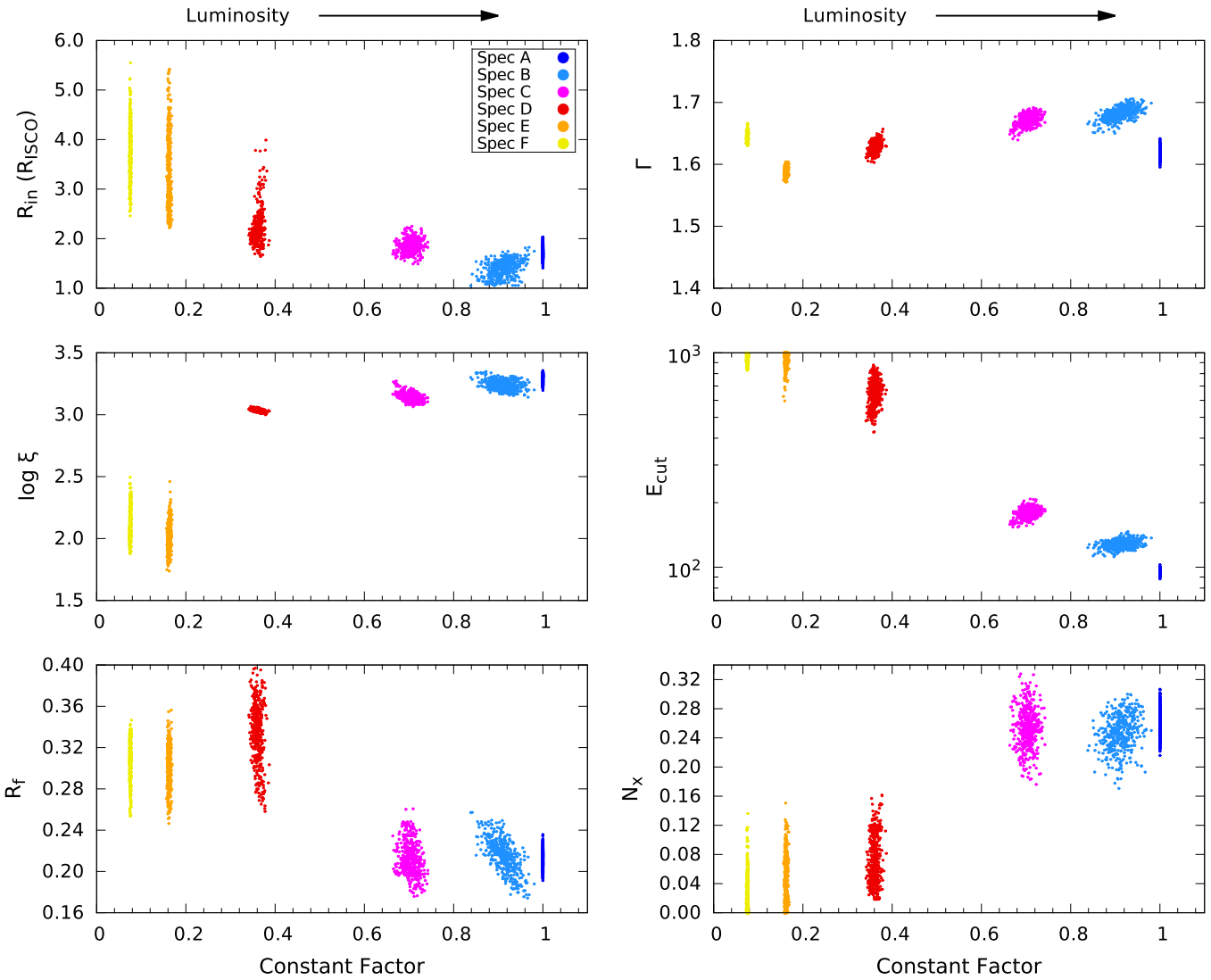

Figure 10. Variation of key model parameters with X-ray luminosity. The clouds of points in each panel (color-coded to correspond to a particular one of the six spectra) show the posterior density of the MCMC results for: the inner radius R_{in} in units of the ISCO radius; the photon index Γ of the power law; the ionization parameter ξ; the high-energy cutoff E_{cut}; the reflection fraction R_f; and the normalization N_x of the unblurred reflection component `xillver`. The Constant Factor on the x-axis, which is proportional to the Eddington-scaled luminosity, is normalized to unity (corresponding to $L/L_{Edd} = 17\%$) for Spectrum A (Table 1).

6.2. Parameters That Evolve Systematically with Luminosity

Setting aside the Gaussian absorption component (already discussed in Section 4), for JF-I there are six important parameters that are fitted separately for Spectra A–F: the inner-disk radius R_{in}; the photon index Γ; the ionization parameter ξ; the high-energy cutoff E_{cut}; the reflection fraction R_f; and the normalization of the unblurred reflection component (`xillver`). In this section, we show how these parameters depend on luminosity, and we discuss the causes of these dependencies.

Figure 10 illustrates our MCMC results for JF-I (Table 3), the case of fixed spin. The probability distribution for each parameter is shown plotted versus the floating constant factor, which can be regarded as a proxy for the luminosity. The luminosity ranges over somewhat more than an order of magnitude. Each Spectrum is color-coded (see legend in top-left panel). The breadth of a distribution is a measure of uncertainty, while its shape indicates the degree of correlation of that particular parameter with luminosity. We now discuss in turn the behavior of each parameter.

6.3. Inner Edge of the Disk

The evolution of the inner-disk radius R_{in} with luminosity is shown in the top-left panel of Figure 10. Each spectrum delivers a good constraint on R_{in}, allowing us to conclude that the inner edge of the disk moves outward by a factor of a few as the luminosity decreases by an order of magnitude, from a nominal value of 17% of Eddington to 1.6% of Eddington (Table 1).

This is a principal result of our paper because R_{in} and its dependence on luminosity is a matter of central importance for the study of black hole binaries in the hard state (Section 1.1). In Table 5 we summarize estimates of R_{in} in the literature for GX 339–4 in the hard state, while considering only those results obtained via reflection spectroscopy. The compilation includes results obtained using a wide variety of data and over

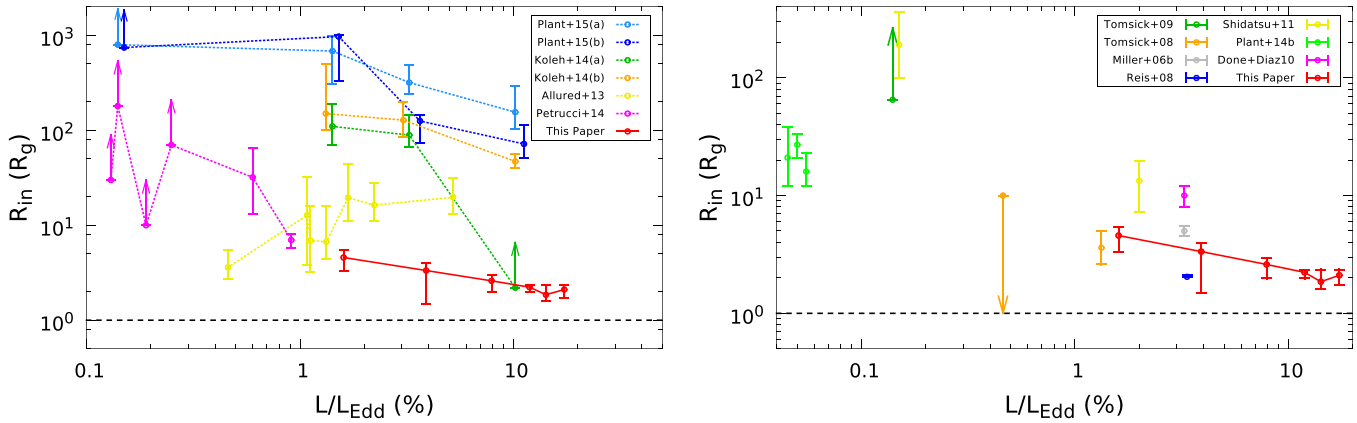

Figure 11. Comparison for GX 339–4 of our estimates with those in the literature (see Table 5) of the inner-disk radius vs. luminosity obtained by reflection modeling of hard-state spectra. The solid red track shown in both panels links our six measurements of $R_{\rm in}$ (Table 3). (*Left*) The various colored tracks show the evolution of $R_{\rm in}$ with Eddington-scaled luminosity (see footnote to Table 1) reported by us and others (Table 5). Plant et al. (2015) and Kolehmainen et al. (2014) each present a pair of tracks, which are labeled `(a)` and `(b)`; the latter track in the case of Kolehmainen et al. (2014) includes a notch feature at ∼9 keV. (*Right*) Single measurements of $R_{\rm in}$ reported in a variety of studies (Table 5). The track labeled `Done+Diaz10` corresponds to results reported by Done & Diaz Trigo (2010) for fits to Epic-pn data. Data points with identical values of luminosity are slightly offset for clarity (precise values are given in Table 5).

a large range in luminosity (∼0.1%–20% of Eddington). At a glance, one notes the extreme range of values reported for $R_{\rm in}$. The most notable conflict is two grossly disparate values reported for the same *XMM-Newton* observation: Reis et al. (2008) analyzed MOS and *RXTE* PCA data and reported $R_{\rm in} = 2.04^{+0.07}_{-0.02}\ R_g$, while Plant et al. (2015) analyzed EPIC-pn timing-mode data and reported $R_{\rm in} = 318^{+165}_{-74}\ R_g$.

Figure 11 shows all the values of $R_{\rm in}$ that appear in Table 5 plotted as a function of the Eddington-scaled luminosity. Several studies report results for multiple observations over a range of luminosity; in these cases, the individual data points are highlighted in the left panel of Figure 11 using colored tracks. Meanwhile, individual measurements are shown in the right panel. Our results are shown in both panels with a solid red track connecting the data points. As noted above, we find that $R_{\rm in}$ increases modestly with decreasing luminosity: Best-fit values trend upward from $2.1\,R_g$ to $4.6\,R_g$ as the luminosity decreases from 17% to 1.6% of Eddington. (Note that the values of $R_{\rm in}$ in Table 3 are in units of $R_{\rm ISCO} = 1.237\,R_g$.)

This trend is consistent with that found in previous studies except for that of Allured et al. (2013) (yellow track), who fitted *Swift* and *RXTE* data using the `reflionx` model. Despite the general agreement that the inner radius shrinks with increasing luminosity, our estimates of $R_{\rm in}$ at comparable values of luminosity are much smaller than those reported by others.

For example, Plant et al. (2015) found the disk to be extremely truncated based on fits to a *Suzaku* and three *XMM-Newton RXTE* spectra using `xillver` and `reflionx` (light and dark blue tracks). Kolehmainen et al. (2014) reported a similar trend but smaller values of radius (green track) by analyzing the same three *XMM-Newton* spectra (excluding the *RXTE* data) using the `rfxconv` model (based on the `reflionx` tables; Kolehmainen et al. 2011). For their highest-luminosity data, they report two values of inner radius: One is a lower limit that is consistent with our results, $R_{\rm in} > 2.2R_g$, while the other (which includes a ∼9 keV instrumental feature in the fit; orange track) is reasonably consistent with the results of Plant et al. (2015), $R_{\rm in} \approx 47\,R_g$. Overall, the results of Kolehmainen et al. (2014) and Plant et al. (2015) are similar,

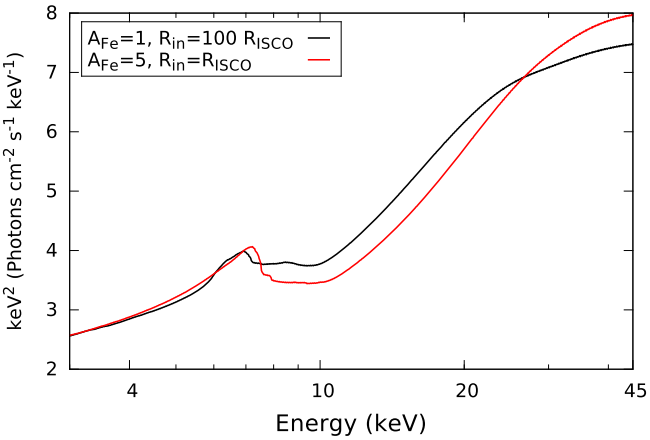

Figure 12. Comparison of two reflection models calculated using our `relxill` code: The red curve is for the parameters of JF-I (see Table 3), in particular for $A_{\rm Fe} = 5$ and $R_{\rm in} = R_{\rm ISCO}$. The black curve is for a model with solar abundances ($A_{\rm Fe} = 1$) that has been doctored by increasing $R_{\rm ISCO}$ by 100-fold to best match the structure in the Fe K line. Meantime, the models are seen to differ greatly in the depth and structure of the Fe K edge and in the shape of the Compton hump.

with the former authors reporting somewhat smaller values of $R_{\rm in}$. Interestingly, our results appear to be in reasonable agreement with an extrapolation of the low-luminosity values of $R_{\rm in}$ reported by Petrucci et al. (2014) (purple track), which is not necessarily expected since these authors assumed solar Fe abundance.

Though the gross disparities in the reported values of $R_{\rm in}$ may be partially due to differences in the models, this should be a secondary effect since, e.g., tests show that the models `xillver` and `reflionx` perform similarly (García et al. 2013). The more likely reason for the inconsistent results is limitations of the data. One of the most severe of these is the effects of pileup, especially for the crucial *XMM-Newton* data (see Section 6.1.3). Another effect leading to major differences in results is whether or not high-energy data were used. For example, Plant et al. (2015) and Kolehmainen et al. (2014) used the same EPIC-pn data in timing mode, but while Plant et al.

Table 6
Coronal Properties[a]

Box	$L/L_{\rm Edd}$ (%)	$E_{\rm cut}$ (keV)	T_e (10^9 K)	$\tau_{\rm e}$
A	17.3	97	0.45	3.03
B	14.2	129	0.60	2.50
C	11.9	179	0.83	1.99
D	7.9	660	3.06	0.72
E	3.9	840	3.90	0.59
F	1.6	890	4.13	0.56

Note.
[a] Assumes $kT = \frac{2}{5}E_{\rm cut}$ and $\Gamma = 1.6$ (See Equation (1)).

(2015) used simultaneous *RXTE* data to extend the energy coverage, Kolehmainen et al. (2014) eschewed its use because of their concern over the cross-calibration of the two detectors. As a consequence of employing *XMM-Newton* data only, the results of Kolehmainen et al. (2014) are highly sensitive to calibration issues associated with the rapidly falling and uncertain response of the EPIC-pn detector at energies $\gtrsim$9 keV.

The PCA has important advantages despite its limited energy resolution and lack of coverage below 3 keV. Most notably, the PCA data are free from the contentious effects of pileup that are inherent to CCD observations of bright sources. Meanwhile, the use of a single detector eliminates problems associated with cross-calibrating a pair of detectors. The much higher effective area of the PCA around the Fe line and Compton hump–and the many dozens of observations—yields spectra with orders-of-magnitude more counts than CCD spectra (Section 5). Moreover, one can now fully utilize these many millions of counts per spectrum to detect subtle effects in reflection features because the response of the PCA has been successfully calibrated to ∼0.1% precision (Shaposhnikov et al. 2012; García et al. 2014b). These virtues of the PCA data are attested to by our success in fitting our reflection models ($\chi^2_\nu \sim 1$) to six extremely high signal-to-noise spectra, which individually contain between 3 and 28 million total counts in the 3–10 keV band. Finally, the great abundance of data makes the PCA database unrivaled for synoptic studies of Galactic black holes.

We now return to the question of the grossly discrepant results reported for $R_{\rm in}$ (Table 5; Figure 11) while reminding the reader that the Fe abundance affects the Fe K line profile and other reflection features at a detectable level given our signal to noise (Section 6.1.4). In turn, the Fe abundance affects other parameters, notably the inner-disk radius and spin parameter, which correlates positively with Fe abundance (Section 6.1.3). We now show that values of $R_{\rm in}$ found by others are significantly biased by either the low signal-to-noise of their data or inadequate high-energy coverage. Such data make it difficult to distinguish between small $R_{\rm in}$ with large $A_{\rm Fe}$ and large $R_{\rm in}$ with solar abundances, as we illustrate in Figure 12, which compares fits to two `relxill` models, one with $A_{\rm Fe} = 1$ and the other with $A_{\rm Fe} = 5$. The model with solar abundance (black curve) can only fit the data when the disk is strongly truncated, which serves to minimize the relativistic effects that blur the line profile. Note, however, that this model then fails to reproduce the depth of the Fe K edge and underpredicts the continuum above ∼30 keV. Figure 12 should be compared directly with Figure 9, where the limitations of the $A_{\rm Fe} = 1$ model are apparent from the fit residuals. Unlike most other data sets, the extreme signal in our data clearly discriminates between the two models.

The truncation of the inner disk and the decrease in $R_{\rm in}$ with increasing $L/L_{\rm Edd}$, which we find, is a prediction of the ADAF model (see Section 1.1). In this paradigm, the inner disk evaporates becoming a very hot and optically thin accretion flow that fills the inner region (see, e.g., Meyer-Hofmeister et al. 2009). Our results are in line with this model, although our observations do not extend to the lower luminosities at which extreme truncation likely occurs.

However, we note that these results are apparently at odds with our non detection of a thermal disk component of emission. Making the usual assumption that all the observed power-law photons are generated by Compton up-scattering of disk photons, we would have expected to detect a thermal component for a disk that extends to such small radii (see Section 7).

6.4. Parameters of the Continuum: Γ and E_{cut}

We find that the power-law photon index Γ is relatively constant despite the order of magnitude increase in luminosity (top-right panel of Figure 10), a result that has been previously reported for GX 339–4 (e.g., Wilms et al. 1999; Zdziarski et al. 2004; Plant et al. 2014a). Its average value is 1.640 ± 0.035 for JF-I and 1.625 ± 0.030 for JF-II (std. dev., $N = 6$; Tables 3 and 4), firmly in the range for the hard state ($1.4 < \Gamma < 2.1$; Remillard & McClintock 2006).

In contrast to the constancy of the power-law index, the cutoff energy $E_{\rm cut}$ systematically decreases with increasing luminosity from >890 keV for Spectrum F down to 97 ± 4 keV for Spectrum A (right-middle panel of Figure 10). This lower value of $E_{\rm cut}$ for our highest luminosity spectrum is of the same order of magnitude as the 58.5 ± 2.2 keV value reported by Droulans et al. (2010), which is based on their analysis of simultaneous *RXTE* and *INTEGRAL* data obtained during another bright hard state of GX 339–4.

Our model achieves good constraints for all six spectra. Remarkably, this is true for even the lowest-luminosity data (Spectrum F) for which the cutoff energy of >890 keV is far beyond the 45 keV limit of the PCA bandpass. This surprising result is a consequence of the detectable effects that are imprinted on the reflected component in the 3–45 keV band by photons with energies of hundreds of keV. We discuss the capability of the `relxill` model to probe the spectrum at extreme energies in Garcia et al. (2015).

In a Comptonized and isothermal corona, the high-energy cutoff is set by the electron temperature: $E_{\rm cut} \sim (2\text{–}3)kT_{\rm e}$. In such a plasma, thermal disk photons are Compton up-scattered, thereby cooling the coronal electrons while producing the observed power-law continuum. The slope of the power law depends on the interplay between the electron temperature and the optical depth $\tau_{\rm e}$,

$$\Gamma = -\frac{1}{2} + \sqrt{\frac{9}{4} + \frac{1}{\theta_{\rm e}\tau_{\rm e}\left(1 + \tau_{\rm e}/3\right)}}, \qquad (1)$$

(Lightman & Zdziarski 1987), where $\theta_{\rm e} = kT_{\rm e}/m_{\rm e}c^2$ and $m_{\rm e}c^2 = 511$ keV is the electron rest mass. Values of these parameters for Spectra A–F, which are consistent with previous determinations (e.g., Wilms et al. 1999), are summarized in Table 6 for our nominal value of the photon index ($\Gamma = 1.6$). We find, as predicted by Equation (1), that the coronal

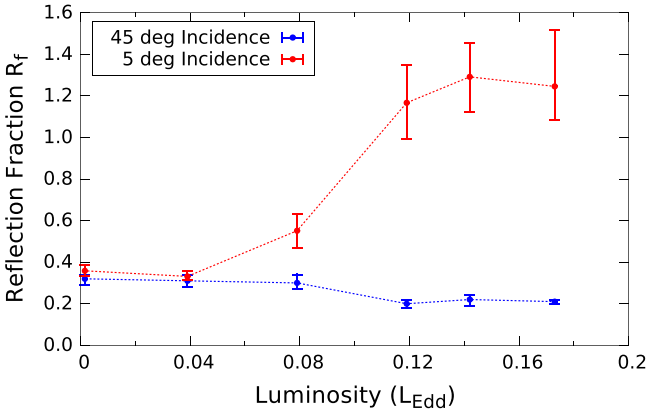

Figure 13. Comparison of the reflection fraction vs. luminosity for two fixed values of the incident angle of the illuminating radiation: the 45° value (blue points), which is widely assumed in reflection modeling, and 85° (red points), the value we have assumed for this test.

temperature decreases with increasing luminosity, while the optical depth increases.

6.5. The Reflection Fraction

The reflection fraction R_f is a third parameter (in addition to Γ and E_{cut}) that provides information on the structure of the corona. In `relxill`, the parameter is empirically defined as the ratio of the reflected flux to the power-law flux in the 20–40 keV band. The results of JF-I show that the reflection fraction of the relativistically blurred component (`relxill`) ranges from $0.2 \lesssim R_f \lesssim 0.3$, decreasing modestly with increasing luminosity (bottom-left panel, Figure 10). This trend is surprising given that, at the same time, R_{in} is decreasing so that the area of the reflector should increase. As a further wrinkle, one expects $R_f \gtrsim 1$ based on simple arguments (Dauser et al. 2014).

There are several scenarios that can plausibly account for values of $R_f < 1$. We mention four and then discuss a new, alternative explanation. (1) An obvious explanation is a severely truncated disk (more specifically, a disk with truncation radius large compared to the size of the corona). We discard this possibility as inconsistent with the small values we find for R_{in} (Section 6.3). (2) Another option is for the corona to be continuously outflowing at relativistic speeds, beaming the bulk of its emission away from the disk (e.g., Miller et al. 2015; Keck et al. 2015). While this is a possible explanation for $R_f < 1$, one outcome of this scenario is a resultant low value of the emissivity index, which is not obviously required by our data. (3) The value of R_f may be depressed by our assumption of a constant-density disk atmosphere, as Ballantyne et al. (2001) have shown in their studies of hydrostatic atmospheres. The hotter gas layer at the surface of a hydrostatic atmosphere additionally scatters and blurs reflection features (see also Nayakshin & Kallman 2001) thereby diluting the reflection signal relative to a constant density model. (4) The apparent strength of reflection features may also be reduced by the Comptonization of these features in an extended corona, as Wilkins & Gallo (2015) recently proposed. However, for such a corona to be effective in reducing R_f appreciably, it must have a large covering fraction which may interfere with detection of blurred reflection features from the inner disk.

We propose an alternative explanation for $R_f < 1$ based on the strong dependence of the reflected spectrum on the angle at which an illuminating photon strikes the disk. This angle crucially determines the characteristic depth in the disk at which the photon interacts; this in turn affects the limb-darkening/brightening of the disk (Svoboda et al. 2009; García et al. 2014a). A deficiency of `reflionx`, `relxill`, `xillver` and other widely used reflection models is the simplifying assumption of a fixed incidence angle of 45°. However, a larger angle of incidence (measured with respect to the normal to the disk plane), for example, results in a hotter surface layer and therefore a weaker reflection signature (see Figure 5 in Dauser et al. 2013).

To test whether the assumption of near-grazing illumination substantially increases fitted values of R_f, we produced a new table of `xillver` reflection models with a fixed incidence angle of 85° and merged them with RELLINE to create a new high-incidence-angle version of `relxill` (Section 1.2). Fitting Spectra A–F as in Section 5.1 (i.e., JF-I), the fit is slightly worse ($\Delta\chi^2 = 9.71$) but statistically comparable and still quite reasonable ($\chi^2_\nu = 1.09$). Notably, for the 85° model we find that R_f increases with luminosity and that $R_f > 1$ for the three most luminous spectra (A–C). Meanwhile, all the other parameters are consistent with those for JF-I (Table 3). Importantly, the Fe abundance remains unchanged.

Figure 13 compares the reflection factors computed for the two models. The large-angle model is more in accord with expectation, namely, the reflection fraction trends upward with luminosity and the values at the higher luminosities (with R_{in} near the ISCO and with correspondingly large reflector area) are sensibly $\gtrsim$1. Thus, our results qualitatively suggest that the accretion disk in GX 339–4 is illuminated at near-grazing angles with respect to the surface of the disk.

Within a few gravitational radii of the horizon, the extreme bending of light rays causes photons to strike the disk over a wide range of angles (Dauser et al. 2013; see in particular the middle panel of their Figure 5). Given the strong dependence of R_f on the angle of incidence, reaching firm conclusions concerning the reflection factor will require building a new generation of models, a task beyond the scope of this paper that will be addressed in future work.

6.6. Ionization Parameter and Geometry

As expected, both the normalization N_r and the ionization parameter ξ of the blurred reflection component (`relxill`) increase with luminosity (Table 3; Figure 10, middle-left panel). In particular, the ionization parameter changes from $\xi = 112.2$ to $\xi = 2041.7$, which traces very well the ten-fold increase in luminosity, from 1.6% L_{Edd} to 17% L_{Edd}. For the strongly illuminated portion of the disk, the variations in ξ and L deviate mildly from the simple relation $\xi = L/nD^2$, where n is the density of the gas (fixed at $n = 10^{15}\,\mathrm{cm}^{-3}$ for the `relxill` and `xillver` models used here)[8], and D is the distance from the coronal source to the strongly heated portion of the disk. Thus, D increases only modestly as the luminosity decreases by an order of magnitude in passing from Spectrum

[8] The choice of gas density is relatively unimportant; it is the ionization parameter that largely determines the properties of the reflected spectrum (see García & Kallman 2010; García et al. 2013).

A to Spectrum F:

$$\frac{D_F}{D_A} = \sqrt{\frac{L_F \xi_A}{L_A \xi_F}} \sim 1.3. \quad (2)$$

This small change is reasonable given the correspondingly mild increase in the inner radius obtained for JF-I:

$$\frac{R_F}{R_A} = 2.2. \quad (3)$$

Likewise, the normalization N_x of the unblurred reflection component (`xillver`) increases with luminosity (Figure 10, bottom-right panel); although presumably the ionization parameter of this component also increases with luminosity, we approximate the state of the gas in the distant reflector as cold and neutral.

7. SUMMARY AND CONCLUSIONS

We have presented an analysis of six composite *RXTE* PCA spectra of the X-ray binary black hole GX 339–4. All these spectra were taken when the source was in the hard state. The spectra correspond to luminosities ranging from 1.6% to 17% of the Eddington luminosity. The six spectra, each spanning the energy range 3–45 keV, comprise in total 77 million counts and a total exposure time of 196 ks. A unique feature of this work is our use of the tool PCACORR, which allows us to calibrate the PCA data to a precision of 0.1%.

The spectra individually, and jointly, are well fitted by a model with three principal components: `relxill`, our model of relativistic ionized reflection; `xillver`, a minor component that models the effects of a cold, distant reflector; and `Tbabs`, a standard model of Galactic absorption. We include an ad hoc Gaussian component (`gabs`) to model an absorption feature near 7 keV. The origin of this feature is unclear, but it is likely an artifact resulting from a misestimate of the PCA energy resolution.

We performed two joint fits of the six spectra. In the first of these, we fixed the spin to its maximal value, which allows the inner-disk radius $R_{\rm in}$ to approach the ISCO radius, and we derived precise estimates for the evolution of $R_{\rm in}$ with luminosity. We find that the disk becomes increasingly truncated with decreasing luminosity. Specifically, as the luminosity ranges from 17% to 1.6% of Eddington, $R_{\rm in}$ increases from $2.1\,R_g$ to $4.6\,R_g$. While this trend has been previously reported (e.g., Kolehmainen et al. 2014; Petrucci et al. 2014; Plant et al. 2015), our values of $R_{\rm in}$ for comparable values of luminosity are much smaller than those found by others. The grossest discrepancy is the hundredfold larger values reported by Plant et al. (2015).

That we find such small values of the inner-disk radius and no evidence for a thermal disk component is at odds with the current models. This is particularly true for Spectrum A with $R_{\rm in} = 2.1\,R_g$. One expects such a modestly truncated disk to be sufficiently hot (particularly because it is heated by the corona; e.g., Haardt & Maraschi 1993) that we should have detected it with the PCA. This implies that our model somewhat underestimates the true value of $R_{\rm in}$ and that our model is incomplete. To address this problem, we are in the process of exploring an extended model that self-consistently treats the thermal, power-law and reflected components. This is a challenging problem whose solution is beyond the scope of this paper.

Our analysis indicates that the factor of ∼100 range in the values of $R_{\rm in}$ at fixed luminosity, which have been reported in the literature, is unlikely to result from the use of different reflection models; the shifts in $R_{\rm in}$ attributable to this cause appear to be relatively minor. Instead, the large disparity appears to be attributable to limitations of the data, one of which is the well-known effects of pileup. In this paper, we highlight a particularly important effect, namely, the modest statistical quality of most data, which has resulted in observers fitting the blurred reflection component assuming that the Fe abundance is solar, whereas we demonstrate that super-solar Fe abundance is required for fits to data with extreme statistical precision. Specifically, we strongly constrain the Fe abundance (in solar units) to be $A_{\rm Fe} = 5.0^{+1.2}_{-0.4}$, which is the average value for our two joint fits. This strict requirement of the data is a promising and likely explanation for why, at luminosities ∼1% of Eddington, we find evidence for relatively mild disk truncation compared to earlier studies.

We acknowledge that the accuracy of our results are limited, systematically, by the presence of an absorption feature near 7.2 keV (Section 4.1) whose origin is unknown. However, our principal conclusions regarding the inner radius of the disk are sound, being subject to a minor uncertainty of about 20% arising from whether or not this feature is included in the model.

As the source luminosity and the radiation field bathing the disk grow, the disk becomes increasingly ionized and its structure changes as $R_{\rm in}$ shrinks. At the same time, the large and steady decrease in the high-energy cutoff indicates that the illuminating coronal source is likewise evolving, as its temperature drops and its optical depth increases.

In the second of our two joint fits to the six spectra, we made the standard assumption used in estimating black hole spin, namely, we fixed $R_{\rm in}$ to the radius of the ISCO. Doing so, we constrained the spin of the black hole to be $a_* = 0.95^{+0.03}_{-0.05}$. We were able to achieve this statistical precision despite the limited spectral resolution of the PCA because of the quality of the data and its calibration.

If there is some truncation of the inner disk (i.e., $R_{\rm in} > R_{\rm ISCO}$), then the spin is greater than the estimate given above. Our estimate of spin agrees well with previous determinations made using the Fe line method (Miller et al. 2004, 2006b, 2008; Reis et al. 2008). It is, however, inconsistent with the upper limit of $a_* < 0.9$ derived using the continuum-fitting method (Kolehmainen & Done 2010), a result that is uncertain because the accurate values of black hole mass, disk inclination and distance that are required for successfully applying the continuum-fitting method are unknown for GX 339–4. Our result is also formally incompatible with the value of spin predicted for GX 339–4 by Steiner et al. (2013) based on the relationship between spin and jet power proposed by Narayan & McClintock (2012), which has been challenged by Russell et al. (2013).

We also obtain a precise estimate for the inclination of the inner disk of $i = 48.1^{+1.0}_{-1.3}$ deg. This value is further subject to an estimated systematic uncertainty of about 4° arising from whether or not one chooses to include the 7.2 keV absorption feature in the model. Our value is inconsistent with the low values found earlier using the Fe-line method (Miller et al. 2004, 2006b, 2008; Reis et al. 2008), while it is more in line with reasonable expectations for the mass of the black hole based on the value of the mass function.

We thank Felix Fürst, Michael Nowak, Timothy Kallman, Rubens Reis, Francesco Tombesi, Andrzej Zdziarski, and Jon Miller for useful and valuable discussions. JG and JEM acknowledge the support of NASA grant NNX11AD08G. J. F. S. has been supported by NASA Hubble Fellowship grant *HST*-HF-51315.01. V. G. acknowledges support provided by NASA through the Smithsonian Astrophysical Observatory (SAO) contract SV3-73016 to MIT for support of the *Chandra* X-Ray Center (CXC) and Science Instruments; CXC is operated by SAO for and on behalf of NASA under contract NAS8-03060.

Facility: RXTE.

REFERENCES

Allured, R., Tomsick, J. A., Kaaret, P., & Yamaoka, K. 2013, ApJ, 774, 135
Anders, E., & Grevesse, N. 1989, GeCoA, 53, 197
Ballantyne, D. R., Ross, R. R., & Fabian, A. C. 2001, MNRAS, 327, 10
Bardeen, J. M., Press, W. H., & Teukolsky, S. A. 1972, ApJ, 178, 347
Corbel, S., Coriat, M., Brocksopp, C., et al. 2013, MNRAS, 428, 2500
Corbel, S., Fender, R. P., Tzioumis, A. K., et al. 2000, A&A, 359, 251
Dauser, T., García, J., Parker, M. L., Fabian, A. C., & Wilms, J. 2014, MNRAS, 444, L100
Dauser, T., Garcia, J., Wilms, J., et al. 2013, MNRAS, 430, 1694
Dauser, T., Svoboda, J., Schartel, N., et al. 2012, MNRAS, 422, 1914
Dauser, T., Wilms, J., Reynolds, C. S., & Brenneman, L. W. 2010, MNRAS, 409, 1534
Done, C., & Diaz Trigo, M. 2010, MNRAS, 407, 2287
Done, C., Gierliński, M., & Kubota, A. 2007, A&ARv, 15, 1
Droulans, R., Belmont, R., Malzac, J., & Jourdain, E. 2010, ApJ, 717, 1022
Dunn, R. J. H., Fender, R. P., Körding, E. G., Belloni, T., & Cabanac, C. 2010, MNRAS, 403, 61
Fabian, A. C. 2006, AN, 327, 943
Fabian, A. C., Wilkins, D. R., Miller, J. M., et al. 2012, MNRAS, 424, 217
Farr, W. M., Sravan, N., Cantrell, A., et al. 2011, ApJ, 741, 103
Foreman-Mackey, D., Hogg, D. W., Lang, D., & Goodman, J. 2013, PASP, 125, 306
Fragos, T., Tremmel, M., Rantsiou, E., & Belczynski, K. 2010, ApJL, 719, L79
Fuerst, F., Nowak, M. A., Tomsick, J. A., et al. 2015, ApJ, 808, 122
García, J., Dauser, T., Lohfink, A., et al. 2014a, ApJ, 782, 76
García, J., Dauser, T., Reynolds, C. S., et al. 2013, ApJ, 768, 146
García, J., & Kallman, T. R. 2010, ApJ, 718, 695
García, J., Kallman, T. R., & Mushotzky, R. F. 2011, ApJ, 731, 131
Garcia, J. A., Dauser, T., Steiner, J. F., et al. 2015, ApJL, 808, L37
García, J. A., McClintock, J. E., Steiner, J. F., Remillard, R. A., & Grinberg, V. 2014b, ApJ, 794, 73
Gierliński, M., & Done, C. 2004, MNRAS, 347, 885
Haardt, F., & Maraschi, L. 1993, ApJ, 413, 507
Hynes, R. I., Steeghs, D., Casares, J., Charles, P. A., & O'Brien, K. 2003, ApJL, 583, L95
Jahoda, K., Markwardt, C. B., Radeva, Y., et al. 2006, ApJS, 163, 401
Kalberla, P. M. W., Burton, W. B., Hartmann, D., et al. 2005, A&A, 440, 775
Kallman, T., & Bautista, M. 2001, ApJS, 133, 221
Kara, E., Fabian, A. C., Lohfink, A. M., et al. 2015, MNRAS, 449, 234
Keck, M., Brenneman, L. W., Ballantyne, D. R., et al. 2015, ApJ, 806, 149
Kolehmainen, M., & Done, C. 2010, MNRAS, 406, 2206
Kolehmainen, M., Done, C., & Díaz Trigo, M. 2011, MNRAS, 416, 311
Kolehmainen, M., Done, C., & Díaz Trigo, M. 2014, MNRAS, 437, 316
Kong, A. K. H., Homer, L., Kuulkers, E., Charles, P. A., & Smale, A. P. 2000, MNRAS, 311, 405
Lightman, A. P., & Zdziarski, A. A. 1987, ApJ, 319, 643
Markert, T. H., Canizares, C. R., Clark, G. W., et al. 1973, ApJL, 184, L67
McClintock, J. E., Narayan, R., & Steiner, J. F. 2014, SSRv, 183, 295
McClintock, J. E., Shafee, R., Narayan, R., et al. 2006, ApJ, 652, 518
Méndez, M., & Klis, v. d. 1997, ApJ, 479, 926
Meyer-Hofmeister, E., Liu, B. F., & Meyer, F. 2009, A&A, 508, 329
Miller, J. M., Homan, J., & Miniutti, G. 2006a, ApJL, 652, L113
Miller, J. M., Homan, J., Steeghs, D., et al. 2006b, ApJ, 653, 525
Miller, J. M., Raymond, J., Fabian, A. C., et al. 2004, ApJ, 601, 450
Miller, J. M., Raymond, J., Homan, J., et al. 2006c, ApJ, 646, 394
Miller, J. M., D'Aì, A., Bautz, M. W., et al. 2010, ApJ, 724, 1441
Miller, J. M., Tomsick, J. A., Bachetti, M., et al. 2015, ApJL, 799, L6
Miller, L., Turner, T. J., & Reeves, J. N. 2008, A&A, 483, 437
Narayan, R., & McClintock, J. E. 2008, NewAR, 51, 733
Narayan, R., & McClintock, J. E. 2012, MNRAS, 419, L69
Narayan, R., & Yi, I. 1994, ApJL, 428, L13
Nayakshin, S., & Kallman, T. R. 2001, ApJ, 546, 406
Neilsen, J., Petschek, A. J., & Lee, J. C. 2012, MNRAS, 421, 502
Özel, F., Psaltis, D., Narayan, R., & McClintock, J. E. 2010, ApJ, 725, 1918
Penna, R. F., McKinney, J. C., Narayan, R., et al. 2010, MNRAS, 408, 752
Petrucci, P.-O., Cabanac, C., Corbel, S., Koerding, E., & Fender, R. 2014, A&A, 564, A37
Plant, D. S., Fender, R. P., Ponti, G., Muñoz-Darias, T., & Coriat, M. 2014a, MNRAS, 442, 1767
Plant, D. S., Fender, R. P., Ponti, G., Muñoz-Darias, T., & Coriat, M. 2015, A&A, 573, A120
Plant, D. S., O'Brien, K., & Fender, R. P. 2014b, e-print (arXiv:1411.7411)
Ponti, G., Papadakis, I., Bianchi, S., et al. 2012, A&A, 542, A83
Reis, R. C., Fabian, A. C., & Miller, J. M. 2010, MNRAS, 402, 836
Reis, R. C., Fabian, A. C., Ross, R. R., et al. 2008, MNRAS, 387, 1489
Reis, R. C., Miller, J. M., & Fabian, A. C. 2009, MNRAS, 395, L52
Remillard, R. A., & McClintock, J. E. 2006, ARA&A, 44, 49
Reynolds, C. S. 2014, SSRv, 183, 277
Reynolds, C. S., Brenneman, L. W., Lohfink, A. M., et al. 2012, ApJ, 755, 88
Reynolds, M. T., & Miller, J. M. 2013, ApJ, 769, 16
Reynolds, M. T., Miller, J. M., Homan, J., & Miniutti, G. 2010, ApJ, 709, 358
Ross, R. R., & Fabian, A. C. 2005, MNRAS, 358, 211
Russell, D. M., Gallo, E., & Fender, R. P. 2013, MNRAS, 431, 405
Rykoff, E. S., Miller, J. M., Steeghs, D., & Torres, M. A. P. 2007, ApJ, 666, 1129
Salvesen, G., Miller, J. M., Reis, R. C., & Begelman, M. C. 2013, MNRAS, 431, 3510
Shaposhnikov, N., Jahoda, K., Markwardt, C., Swank, J., & Strohmayer, T. 2012, ApJ, 757, 159
Shidatsu, M., Ueda, Y., Tazaki, F., et al. 2011, PASJ, 63, 785
Steiner, J. F., & McClintock, J. E. 2012, ApJ, 745, 136
Steiner, J. F., McClintock, J. E., & Narayan, R. 2013, ApJ, 762, 104
Steiner, J. F., McClintock, J. E., Remillard, R. A., Narayan, R., & Gou, L. 2009, ApJL, 701, L83
Steiner, J. F., McClintock, J. E., Remillard, R. A., et al. 2010, ApJL, 718, L117
Svoboda, J., Dovčiak, M., Goosmann, R., & Karas, V. 2009, A&A, 507, 1
Tomsick, J. A., Kalemci, E., Kaaret, P., et al. 2008, ApJ, 680, 593
Tomsick, J. A., Yamaoka, K., Corbel, S., et al. 2009, ApJL, 707, L87
Verner, D. A., Ferland, G. J., Korista, K. T., & Yakovlev, D. G. 1996, ApJ, 465, 487
Wilkins, D. R., & Gallo, L. C. 2015, MNRAS, 448, 703
Wilms, J., Allen, A., & McCray, R. 2000, ApJ, 542, 914
Wilms, J., Nowak, M. A., Dove, J. B., Fender, R. P., & Di Matteo, T. 1999, ApJ, 522, 460
Yamada, S., Makishima, K., Uehara, Y., et al. 2009, ApJL, 707, L109
Zdziarski, A. A., Gierliński, M., Mikołajewska, J., et al. 2004, MNRAS, 351, 791
Zhu, Y., Davis, S. W., Narayan, R., et al. 2012, MNRAS, 424, 2504